UNIVERSITY OF CALGARY

Observation of a Planar Isomer of the $N_2O - (C_2H_2)_2$ Trimer

by

Sahar Sheybani-Deloui

A THESIS

SUBMITTED TO THE FACULTY OF GRADUATE STUDIES

IN PARTIAL FULFILMENT OF THE REQUIREMENTS FOR THE

DEGREE OF MASTER OF SCIENCE

DEPARTMENT OF PHYSICS AND ASTRONOMY

CALGARY, ALBERTA

JANUARY, 2014

Abstract

Spectra of clusters of nitrous oxide-acetylene trimer formed in a pulsed supersonic slit-jet expansion have been recorded by exciting the nitrous oxide (N_2O) ν_1 fundamental band (~2224 cm^{-1}) using a quantum cascade laser. High-resolution infrared spectra of the weakly bound N_2O – $(C_2H_2)_2$ trimer were fitted to a semi-rigid asymmetric rotor Hamiltonian. The band is an a/b-type hybrid band with the rotational constants of A =2871.4(11) MHz, B = 1140.67(20) MHz and C = 816.46(14) MHz, satisfying the planarity condition. In addition to the normal istopologue, $^{15}N_2O$ – $(C_2H_2)_2$ and N_2O – $(C_2D_2)_2$ have been also observed to corroborate the determination of the structure.

A cluster calculation program was used to perform semi-empirical calculations on N_2O – $(C_2H_2)_2$ trimer by using the well-known Muenter's distributed multipole potentials and Powell minimization method. According to these calculations, N_2O – $(C_2H_2)_2$ trimer should have a planar structure at the lowest energy minimum which agrees fairly well with the experimental structure.

The two angles between the acetylene and nitrous oxide could not be determined based on the experimental results. The inability to determine these angles may be attributable to the large amplitude motion between the C_2H_2 monomers, which has been observed in C_2H_2 dimer, C_2D_2 dimer and OCS – $(C_2H_2)_2$. The tunneling motion causes the splitting of energy levels. In the spectrum of N_2O – $(C_2H_2)_2$ trimer, no splittings within the resolution of the experiment (75 MHz) are observed that can be attributed to the large amplitude motion between the C_2H_2 monomers.

Acknowledgement

I would like to express my gratitude to all who made this thesis possible. I owe the deepest gratitude to Dr. Nasser Moazzen-Ahmadi. Without his support, guidance, encouragement and persistent help this thesis would not have been possible. My heartfelt appreciation goes to my parents who support and encourage me throughout the entire process. I owe a very important debt to the scientific support and feedback offered by Dr. Jalal Norooz-Oliaee, Mojtaba Rezaee, and Dr. ARW Mckellar. I appreciate the supervisory committee members who kindly accepted to review this thesis and give insightful comments and suggestions. This project was supported by National Sciences and Engineering Research Council of Canada (NSERC), National Research Council of Canada (NRC-CNRC) and Dr. Kirk Michaelian. Also, discussions with my colleagues Mahdi Yousefi Koopaee and Jobin George in Laser Spectroscopy lab at the University of Calgary have been illuminating.

Table of Contents

List of Figures

List of Tables

List of Symbols and Abbreviations

cm	Centre of Mass
CTRO	Counter-Timer Controller
DAQ	Data Acquisition
disp.	Dispersion
es	Electron Spin Magnetic moment
hfs	Hyper-fine-structure
int	Internal
IR	Infrared
OPO	Optical Parametric Oscillator
QCL	Quantum Cascade Laser
rep.	Repulsion
rot.	Rotation
sph	Spherical
trans.	Translation
vdW	van der Waals
vib.	Vibration

Chapter 1: Introduction

Three types of attractive van der Waals forces, which are the main intermolecular forces responsible for forming molecular clusters, are discussed. A brief introduction on infrared spectroscopy of weakly bound molecular clusters is given. The supersonic jet expansion technique which is utilized for formation of molecular clusters is explained. Finally, the objective and organization of this thesis are presented.

1.1 A Review of Weak Intermolecular van der Waals Forces

Molecules are held together in gaseous and condensed states by the intermolecular forces. The intermolecular forces are categorized into four different types: Hydrophobic interaction (between hydrophobes and water molecules), Ionic interaction (between ions in ionic solids), Hydrogen bonding, and van der Waals force. Among the intermolecular forces, ionic interaction is the strongest and van der Waals force is the weakest (See Table 1.1) [1].

Table 1.1: Intermolecular forces energies comparison

Intermolecular Force	Energy (kJ/mol)
van der Waals interaction	0.1-10
Hydrogen bonding	10-40
Hydrophobic interaction	<170
Ionic interaction	100-1000

Weak intermolecular forces are dominated by thermal energy (kT) at room temperature. If the gas molecules or atoms are cooled down, they form a liquid; and, if they are further cooled, they condense into a solid [2]. Weak intermolecular interactions become important when the thermal energy is reduced.

As mentioned above, the weakest intermolecular force among neutral molecules is van der Waals force, which is named after Dutch physicist Johannes Diderik van der Waals (1827-1923). Van der Waals was inspired by Rudolf Julius Emanuel Clausius' 1850 treatise, "On the Moving Force of Heat and the Laws of Heat which may be Deduced Therefrom", to consider heat as a phenomenon of motion which resulted in a search for an explanation of Thomas Andrews' experiments on the existence of critical temperatures in gases [3, 4]. Van der Waals decided that the non-zero size (volume) of molecules and the intermolecular forces should be considered in forming a relationship among the volume (V), temperature (T) and pressure (P) of gases. This equation [3] is given by:

$$\left(P+\frac{a}{V^2}\right)(V-b)=RT \tag{1.1}$$

where R is the universal gas constant; b is a constant and represents the volume occupied by the incompressible molecules, which decreases the available volume to the gas molecules from V to V-b; a is a constant that represents the attraction between molecules; and pressure P decreases by increasing a at constant values for the temperature and volume which verifies the fact that the attraction between molecules reduces the pressure on the container's walls [5].

Van der Waals forces are categorized into three different types: Keesom interactions, Polarization (induction), and London dispersion. As shown in Figure 1.1, Keesom interactions exist among different molecules with permanent dipoles, as a result of their polar bonds. There is an electrostatic force between electric dipoles, so that the molecules align themselves to decrease their energy by increasing the attraction until the repulsion force appears [6].

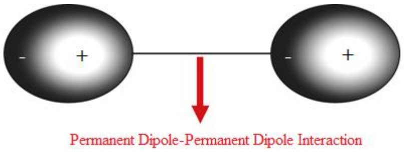

Figure 1.1: Permanent dipole – permanent dipole (Keesom) interaction

Polarization (induction) occurs between a molecule without a permanent dipole moment and a molecule with a permanent dipole moment. As shown in Figure 1.2, a molecule with a permanent dipole leads to an imbalance of electric charge on the molecule without a permanent dipole, which results in creating an induced dipole on this molecule. The molecules are then attracted to each other by this effect [6].

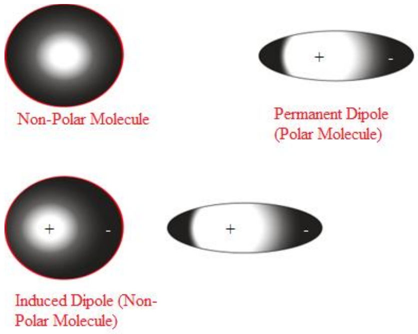

Figure 1.2: Polarization (induction) interaction

Although some molecules do not have a net dipole moment, based on a fluctuation in electron charge densities, the charge imbalance can still occur in non-polar molecules. This leads to an induced dipole on the other molecule, resulting in the attraction of the two molecules, as shown in Figure 1.3, in the same way as polarization. This kind of force is referred to as London dispersion, which is very weak in comparison with Keesom and induction interactions [6].

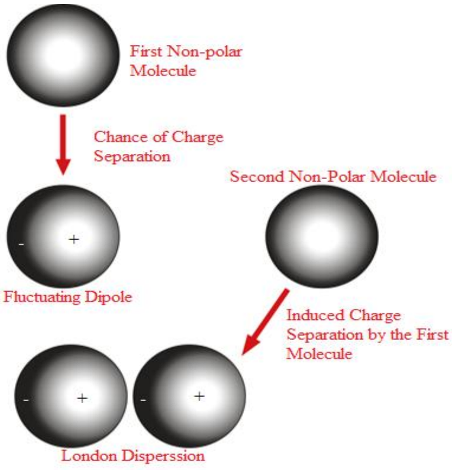

Figure 1.3: London dispersion

Repulsion force dominates at short range which limits the compressibility of matter. At short intermolecular separations there are electrostatic repulsions between the positively charged nuclei of neighbouring molecules and also between negatively charged electron clouds of nearby molecule. The balance between the long range van der Waals force and short range repulsion is characterized by a potential curve with a shallow minimum. The molecules held together in this minimum are called van der Waals molecular clusters. The van der Waals bonds can easily dissociate near the room temperature (~ 300 K); thus, many molecular clusters can be stable only at low temperatures.

Molecular clusters represent intermediate states between the individual isolated molecules in the gaseous state and liquid droplets. Therefore, a better understanding of their properties, such as geometrical arrangements, is of high interest [7].

1.2 A Brief Introduction of Infrared Spectroscopy

A brief history of discovery of infrared radiation is given. Infrared spectroscopy is introduced. Early difficulties in this field are explained. Supersonic jet spectroscopy technique which was used in observation of the planar isomer of N_2O – $(C_2H_2)_2$ and its advantages are discussed.

1.2.1 History

In 1800, the existence of infrared (IR) radiation was recognized by Sir William Herschel (1738-1822) [8]. Herschel had the idea that colours themselves may have different temperatures associated with them, so he performed an experiment where sunlight was directed through a prism to create a rainbow. The temperature of light colour was measured by three thermometers with darkened tubes to better absorb heat. For each colour of the spectrum, one tube in a visible colour was used; and, the other two darkened tubes were used to monitor the ambient temperature.

While measuring the temperatures of the individual colours, he observed that all of the colours' temperatures were higher than the ambient temperature. Additionally, he found that the temperatures increased from the violet part of the spectrum to the red part. He then measured the temperature just beyond the red portion of the spectrum in a region where no sunlight was visible. Surprisingly, he found that this region had the highest temperature. He performed more experiments on this part of the spectrum and noticed that its behaviour (reflection, refraction, absorption, etc.) was similar to visible light. What he found is known as infrared radiation [9].

There were no further investigations on infrared radiation up to the year 1882. In a period of 18 years from 1882 to 1900, the absorption spectra of organic liquids were photographed by Abney and Festing [10]. William Coblentz investigated the spectra of hundreds of organic and inorganic substances, in 1903 [11]. His exploration was the real basis for infrared (IR) spectroscopy.

These early works resulted in the recognition that each compound has distinctive IR spectrum that can be used in characterizing it in different samples, because the absorption bands for each compound were found to be approximately at the same wavelength [12].

Early researchers had many difficulties in conducting their experiments: There were so many problems with analyzing data due to lack of a suitable theoretical framework. Also, there were no suitable light sources such as masers or lasers, and higher sensitive infrared detectors, so early researchers used prisms and broad-band sources of light in their experiments [12]. These difficulties led to design and development of new theories, techniques and instruments such as quantum mechanics, masers and laser, computer-based data acquisition and data analysis, etc. These advances helped to develop high-resolution IR spectroscopy.

1.2.2 Introduction to IR Spectroscopy

IR spectroscopy is a technique that can be used as a versatile method for both the characterization and evaluation of chemicals. This technique is based on a sample's emission or absorption of IR radiation. The absorbed or emitted IR radiation is related to discrete vibrational and/or rotational transitions of molecular samples [13].

Infrared radiation is categorized into three different regions: near IR at 14000–4000 cm^{-1} (0.7–2.5 μm), mid IR at 4000–400 cm^{-1} (2.5–25 μm) and far IR at 400–10 cm^{-1} (25–1000 μm). Their names are indicative of their relation to the visible radiation. Each of these regions is applied for specific studies. Near IR radiation is able to excite molecular harmonic or overtone vibrations, while mid IR is used for studying rotational-vibrational fundamental bands of molecules; and, far infrared, which is near the microwave region, is used in rotational spectroscopy.

High-resolution IR spectroscopy with tunable lasers and modern supersonic jet technique, which is discussed in the next subsection, provides a powerful tool to study the structure and dynamic of the molecular clusters. Studying high resolution IR spectra results in determination of physical parameters such as Coriolis forces, centrifugal distortions, dipole moments, vibrational fundamental frequencies, and intramolecular vibrational relaxation [14].

1.2.3 Introduction to Supersonic Jet Spectroscopy

There is a continuous effort to design and develop new techniques and to increase the versatility and sensitivity of high resolution spectroscopic methods for studying molecular clusters. There are two main issues in IR high-resolution spectroscopy of weakly bound molecular complexes. The primary goal is to generate the desired clusters at a sufficiently low temperature to avoid thermal dissociation, but also producing as many rotational and vibrational lines as can be observed. The second issue is to provide a proper environment that does not have an undesirable effect on the clusters already formed [15].

A supersonic jet meets both these requirements. In this technique, a desirable sample travels perpendicular to the laser beam in free space with a narrow velocity distribution (to decrease Doppler broadening) and a collision free environment (to avoid pressure broadening), so that interactions between the sample and environment are negligible. Supersonic jet expansion works based on adiabatic expansion, which is explained in Chapter 4. Molecules of interest are seeded into a monoatomic carrier gas: this causes the molecules' translational and rotational degrees of freedom to cool to low temperatures, so that the high-lying rotational states have a very small population with concomitant population enhancement in the low-lying rotational states which results in simplification of the rotational structure [15].

1.3 Thesis Study

This thesis discusses the IR spectroscopic studies of a planar isomer of nitrous oxide-acetylene trimer. Supersonic jet expansion was used to form the clusters, and spectra were recorded around ~2232 cm^{-1} using a quantum cascade laser. The focus of this thesis is, therefore, on the analysis of the recoded data, such as the assignment and fitting of the spectra and determination of the structures.

1.3.1 Objective

Previous studies on complexes containing subunits of nitrous oxide (N_2O), acetylene (C_2H_2) and carbonyl sulfide (OCS) show that complexes of these molecules are comparable in structure and symmetry (See Chapter 2). In 2009, the weakly bound N_2O – C_2H_2 and N_2O – C_2D_2 complexes were observed in the (N_2O) ν_1 fundamental band region [16]. It was predicted that this isomer has a near parallel structure with C_s symmetry. Later in the same year, the IR spectra of OCS – C_2H_2 and OCS – C_2D_2 were observed in the OCS ν_1 region [17]. In 2011, a planar isomer of the OCS – $(C_2H_2)_2$ was observed [18], and the structure of this lowest energy isomer was determined to be planar with C_s symmetry. More details of these studies are discussed in Chapter 2. Knowing the geometrical structure of the lowest energy isomer of OCS – $(C_2H_2)_2$ and similarities between the lowest energy isomers of N_2O – C_2H_2 and OCS – C_2H_2 were the inspiration for our investigation of the planar isomer of N_2O – $(C_2H_2)_2$ trimer.

1.3.2 Thesis Organization

This thesis consists of six chapters: Chapter 2 includes previous studies on the related dimers and trimers in terms of the symmetry and geometrical structure. There are no previous experimental or theoretical results published regarding the observation of the IR spectra of N_2O – $(C_2H_2)_2$, but other complexes containing nitrous oxide, acetylene, carbonyl sulfide (OCS), and carbon dioxide (CO_2) have been observed. Chapter 3 outlines the theoretical concepts of vibration-rotation spectroscopy. This background is related to the methods that have been used in the examination and analysis of data. Chapter 4 focuses on the experimental aspects of supersonic jet laser spectroscopy technique. The data acquisition package and related software are discussed. Chapter 5 describes the observation of a planar isomer of N_2O – $(C_2H_2)_2$ trimer. It discusses the analyses done on this complex and the information that has been extracted from the spectra. Finally, Chapter 6 consists of the summary of the experimental studies. Future works are also presented.

Chapter 2: Literature Review

The significance of studying molecular clusters is explained. The previous studies on binary clusters such as N_2O – C_2H_2, OCS – C_2H_2, and CO_2 – C_2H_2 are summarized. The previously studied planar isomer of OCS – $(C_2H_2)_2$, that has a similar structure to N_2O – $(C_2H_2)_2$, is then presented.

2.1 Importance of Studying Molecular Clusters

Weakly bound van der Waals clusters containing two or more monomer units are of fundamental interest in the study of intermolecular interactions. By studying binary clusters or dimers one can directly probe the intermolecular potential in the region of the potential minimum. Ternary clusters or trimers provide information on the two-body potential in new regions as well as non-additive effects on the potential energy surface.

Larger clusters further probe the potential and non-additive effects in new regions. The potential energy surface includes information on possible condensation pathways. There can be many such pathways, since the number of distinct cluster isomers or the local minima in the total potential energy surface grows quickly with cluster size. Many of these clusters are made from simple molecules, e.g. nitrous oxide (N_2O), carbon dioxide (CO_2), carbonyl sulfide (OCS) and acetylene (C_2H_2), some of which are discussed in this literature survey such as nitrous oxide – acetylene (N_2O – C_2H_2), carbon dioxide – acetylene (CO_2 – C_2H_2), carbonyl sulfide – acetylene (OCS – C_2H_2), and carbonyl sulfide – acetylene trimer (OCS – $(C_2H_2)_2$).

2.2 Observation of the Planar Isomer of $CO_2 – C_2H_2$ Dimer

In 1988, Prichard et al. observed the IR absorption spectrum of the $CO_2 – C_2H_2$ van der Waals complex for the first time by exciting the *CH* asymmetric stretch [19]. They found the vibrational origin to be 3281.74 cm^{-1}. Also, the axes of the two monomers were found to be parallel to one another, with the complex having C_{2v} symmetry (See symmetry discussions in Chapter 3).

One year later, Huang, and Miller reported the structural determination of the $CO_2 – C_2H_2$ complex using near infrared laser molecular beam spectroscopy [20]. Their results were in a good agreement with those of Prtichard et al.'s but with higher precision. They determined a structure using recognizable intensity alternations because of the C_2 symmetry axis of this dimer. In the same year, Muenter published an article on the spectra of $CO_2 – C_2H_2$ and $CO_2 – C_2D_2$ clusters [21]. He measured the rotational constants and centrifugal distortion of those clusters. He also measured the dipole moment of $CO_2 – C_2H_2$ and rms vibrational amplitudes and also obtained an estimate of 40 cm^{-1} for the out of plane bending mode [21]. The monomer-monomer stretching vibration was also estimated to be 75 cm^{-1} based on the centrifugal distortion measurement [21].

In 1990, Bone and Handy performed large-scale ab-initio calculations [22] on three dimers formed from C_2H_2 and CO_2 including $(CO_2)_2$, $(C_2H_2)_2$, and $CO_2 – C_2H_2$. They also noted that a co-linear form of $CO_2 – C_2H_2$ is a local minimum on its potential energy surface in addition to the C_{2v} form of that cluster. One year later, Muenter used a general model to describe the intermolecular potential functions for weakly bound molecular complexes: the model was designed to replicate many observed features of the complex [23]. He calculated atom-atom Lennard-Jones terms, electrostatic energies and described repulsion and dispersion with distributed multipole picture of monomer charge distribution (See Chapter 5). He used this model for $CO_2 - C_2H_2$ to calculate the binding energy and vibrational frequency for monomer-monomer stretch and out-of-plane torsional modes.

In 2009, Lauzin et al. studied the $CO_2 - C_2H_2$ van der Waals complex in the $2CH$ overtone region [24]. They observed a perturbed b-type band centered near 6549.28 cm^{-1} and from comparison of the simulated and observed spectra, they found that the rotational temperature is close to 60 K. The overtone data they presented, involved ground state levels with higher J (angular momentum quantum number) and K_a (angular momentum around a axis) in comparison with previously reported data. They combined their data and those of Prichard and Huang to determine improved ground state parameters [19, 20]. c-type Coriolis resonances were found to be the main cause of perturbations influencing the upper state.

Later in 2011, Lauzin et al. observed the IR spectra of the weakly bound $CO_2 - C_2H_2$ dimer in the region of the $(CO_2)\ \nu_3$ fundamental band (~2349 cm^{-1}) [25]. They assigned the spectra to $CO_2 - C_2H_2$ with C_{2v} symmetry and also determined the out-of-plane torsional frequency to be 44.385 cm^{-1} in good agreement with Muenter's prediction of 40 cm^{-1} (Figure 2.1).

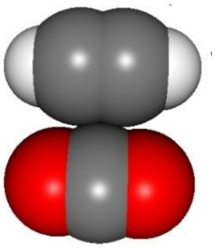

Figure 2.1: Parallel structure of $CO_2 - C_2H_2$ with C_{2v} symmetry parallel to the a intermolecular axis(literature value for van der Waals radii) **[**25**]**

2.3 Previous Studies on the Planar Isomer of N_2O – C_2H_2 Dimer

In 1991, Hu et al. reported the spectra of weakly bound van der Waals clusters of N_2O – C_2H_2 [26]. Using the fact that N_2O and CO_2 are isolectronic, have an identical molecular weight, and nearly equal intramolecular bond length, R_{CO} = 1.16 Å, R_{NN} = 1.13 Å, R_{NO} = 1.1 Å and $(R_{NN}+R_{NO})/2$ = 1.16 Å, they developed a useful potential function model assuming a distributed multipole charge on the monomer [27, 28] and applied it to CO_2 – C_2H_2 complex [23]. They applied the same model to N_2O – C_2H_2 [26]. They studied the region of the acetylene ν_3 fundamental band in the mid-IR region of 3280 cm^{-1} and concluded that the structure is planar, with side-by-side monomer units having approximately parallel monomer axes in agreement with their developed model.

Subsequent studies on N_2O – C_2H_2 in the microwave region [29-31] included a number of isotopic species and resulted in a refined structure with a centre of mass separation of 3.30 Å, and a small angle (13.6°) between the monomer axes, such that the O-atom at the end of the N_2O is located closer to the C_2H_2 axis (Figure 2.2) [31].

Ten years later, Didriche et al. reported the IR observation of N_2O – C_2H_2 in the region of the acetylene 2*CH* asymmetric stretching overtone around 6550 cm^{-1} [32]. They observed and analyzed transitions from higher rotational levels, due to the high rotational temperature (∼15 K) of their jet. However, their effort to analyze the N_2O – C_2H_2 spectrum in the region of the (N_2O) $3\nu_3$ overtone, which is around 6580 cm^{-1}, was not successful because of the weakness of the transitions.

Later in 2009, Dehghany et al. reported the observation of N_2O – C_2H_2 spectra in the region of the (N_2O) ν_1 fundamental band around 2224 cm^{-1} [16]. They observed fundamental and torsional combination bands for both the N_2O – C_2H_2 and N_2O – C_2D_2 isotopomers. This represented the first observation of N_2O – C_2D_2 in the IR region, also the first observation of an intermolecular vibration for the N_2O – C_2H_2 complex (Figure 2.2).

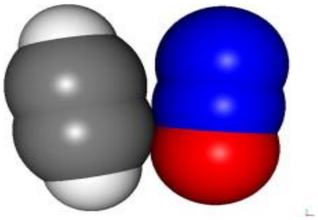

Figure 2.2: Near parallel structure of N_2O – C_2H_2 with C_s symmetry [16]

2.4 Observation of OCS – C_2H_2 Dimer

As mentioned in the introduction of this chapter, OCS – C_2H_2 was studied in the microwave region for the first time. Peebles and Kuczkowski, [33, 34] found that OCS – C_2H_2 has two distinct isomers, including one isomer with a slipped near-parallel geometry (C_s symmetry) and the other with a T-shaped structure (C_{2v} symmetry) with OCS forming the stem of the T and the S-atom interacting with the C_2H_2 triple bond. The structure of the first isomer is similar to that of the previously observed N_2O – C_2H_2 complex. Peebles and Kuczkowski used semi-empirical and ab initio calculations to show that the near-parallel isomer is the lowest energy form of OCS – C_2H_2 [34].

In 2009, Norooz Oliaee et al. reported the first observation of IR spectra of OCS – C_2H_2 [17]. They studied OCS – C_2H_2 and OCS – C_2D_2 isotopomers for the both isomers in the OCS region of the ν_1 fundamental band (~2060 cm^{-1}) and obtained rotational parameters for the excited vibrational state and vibrational shifts due to complex formation (Figure 2.3).

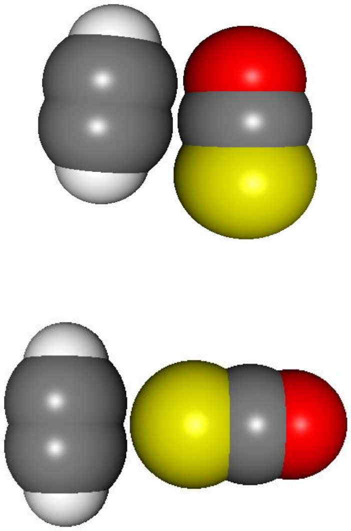

Figure 2.3: Near-parallel structure of the lowest energy isomer of OCS – C_2H_2 with C_s symmetry is shown at the top and T-shaped structure of OCS – C_2H_2 with C_{2v} symmetry is shown at the bottom of the figure. [17]

2.5 Observation of the Planar Isomer of OCS – $(C_2H_2)_2$ Trimer

High resolution spectroscopic investigation of trimers provides information about the effect of adding a third body to the two-body interaction. So, it initiates the study of the many-body interactions by adding a monomer to the clusters. So far, studies of dimers containing N_2O, C_2H_2, CO_2, and OCS were discussed. One of the trimers which was studied based on adding a monomer to the dimer complex is OCS – $(C_2H_2)_2$ which is discussed in this section.

In 2000, Peebles and Kuczkowski observed the pure rotational microwave spectra of four isotopic forms of OCS – $(C_2H_2)_2$ trimer: $^{13}C_2H_2$, $O^{13}CS$, ^{18}OCS, and the normal isotope [35]. The observed spectra revealed an unsymmetrical barrel-shaped structure for this cluster. In this specific structure, C_2H_2 monomers were found to be in an almost planar configuration between T-shaped and parallel arrangements, with the OCS oriented approximately above the plane

(Figure 2.4). However, their results did not agree well with the semi-empirical structure, because some mixed isotopologues (one singly substituted isotopomer: OCS – $H^{13}C^{12}CH$–$H^{12}C^{12}CH$, and two doubly substituted isotopomers: OCS – $H^{13}C^{13}CH$–$H^{12}C^{12}CH$) could not be observed [35]. Because the structural parameters of the trimer could not be determined unambiguously, they concluded that this inability was due to lack of sufficient data and/or the confusion in determining the structure of C_2H_2 dimer unit in the trimer.

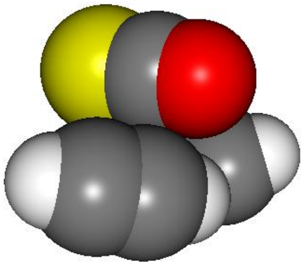

Figure 2.4: Observed isomer of OCS – $(C_2H_2)_2$ by Peebles et al. [35]

Subsequently, Valdés and Sordo performed an ab initio calculation of the OCS – $(C_2H_2)_2$ [36]. They found out that the geometrical structure of C_2H_2 dimer unit in OCS – $(C_2H_2)_2$ is approximately T-shaped but, with a low energy transition state that has a parallel C_2H_2 dimer fragment within the OCS-$(C_2H_2)_2$. Therefore, a relatively large amplitude zero-point motion was found between C_2H_2 monomers. This theoretical work could help to explain the problem in determining the structural parameters for the trimer.

In 2011, Norooz Oliaee et al. reported the first experimental IR observation of planar OCS – $(C_2H_2)_2$, by means of its high-resolution spectrum in the region of the (OCS) ν_1 fundamental band (~2060 cm^{-1}) [18]. They found partial information on the structures of three isotopologues: $^{16}O^{12}C^{32}S$ – $(HCCH)_2$, $^{16}O^{12}C^{32}S$ – $(DCCD)_2$, and $^{18}O^{12}C^{32}S$ – $(DCCD)_2$. Although their results help to increase our understanding of the structure of OCS – $(C_2H_2)_2$, it raises more questions, such as why the planar isomer is observable in IR, while the barrel-shaped configuration is observable in the microwave region (Figure 2.5) [18].

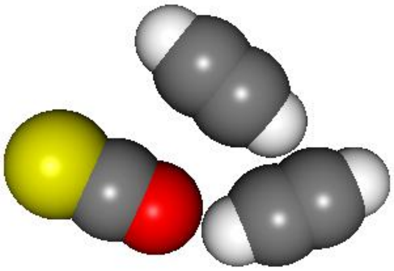

Figure 2.5: Lowest energy isomer of the planar OCS – $(C_2H_2)_2$ with C_s symmetry [18]

Discussions in this chapter show that complexes containing N_2O, C_2H_2, CO_2, and OCS are similar to each other in terms of structure. For instance, both N_2O – C_2H_2 and OCS – C_2H_2 have near parallel structures with C_s symmetry in their lowest energy form. As a result, one can wonder about the structure of the N_2O – $(C_2H_2)_2$ trimer and whether it is similar to that of OCS – $(C_2H_2)_2$.

Chapter 3: Theoretical Concepts

This chapter explains the required theoretical physics for the analysis of the recorded IR spectra. The molecular Hamiltonian is discussed. The rotational constants and molecular symmetry are determined. The probability of tunneling effect in C_2H_2 dimer is also explained.

3.1 Molecular Hamiltonian

The molecular Hamiltonian is defined as the sum of the kinetic energy and potential energy of the particles and interactions of electronic and nuclear spin magnetic or electric moments. Therefore, the Hamiltonian of a molecule can be written as:

$$\hat{H} = \hat{T}_{cm} + \hat{T}' + \hat{T}_0 + \hat{V} + \hat{H}_{es} + \hat{H}_{hfs} \qquad (3.1)$$

In the above equation, the kinetic energy of the centre of the mass of a molecule is denoted by $\hat{T}_{cm}$, intramolecular kinetic energy is shown by $\hat{T}_0$ and $\hat{T}'$ is related to the cross terms of intramolecular kinetic energy. $\hat{V}$ represents the electrostatic potential energy; and, $\hat{H}_{es}$ denotes the interaction between the electronic spin magnetic moments and the magnetic moments caused by the orbital motion of the electron (spin-orbit interaction) or nuclei, or the spin magnetic moment produced by the orbital motion of nuclei (spin-spin interaction). The subscript *hfs* in the last term of the Hamiltonian is the acronym for nuclear hyperfine structure. It arises from the interaction of the electric and magnetic moments of the nuclei with the other electric or magnetic moments of the molecule [37].

In Equation 3.1, the summation of the last three terms can explain the electromagnetic interactions among the particles, while the summation of the last five terms describes the internal molecular Hamiltonian ($\widehat{H}_{int}$), as a result the total Hamiltonian can be rewritten as:

$$\widehat{H} = \hat{T}_{cm} + \widehat{H}_{int} \tag{3.2}$$

Considering Equation 3.1, the sum of $\hat{T}^{0}$, $\hat{T}'$ and V defines the spin free rovibronic Hamiltonian ($\widehat{H}_{rve}$).

$$\widehat{H}_{int} = \hat{T}^{0} + \hat{T}' + V + \widehat{H}_{es} + \widehat{H}_{hfs} = \widehat{H}_{rve} + \widehat{H}_{es} + \widehat{H}_{hfs} \tag{3.3}$$

Equation 3.3 shows that $\widehat{H}_{int}$ does not depend on the coordinate of the centre of mass. Thus the eigenfunction can be separated as:

$$\widehat{H}|\phi\rangle = E|\phi\rangle \tag{3.4}$$

$$\phi = \phi_{cm}(X_0, Y_0, Z_0)\phi_{int}(X_1, Y_1, Z_1 \ldots X_n, Y_n, Z_n) \tag{3.5}$$

If the above relationship is substituted in the Schrodinger equation:

$$\hat{T}_{cm}|\phi\rangle_{cm} = E_{cm}|\phi\rangle_{cm} \tag{3.6}$$

$$\widehat{H}_{int}|\phi\rangle_{int} = E_{int}|\phi\rangle_{int} \tag{3.7}$$

Therefore, it can be concluded that the total energy is:

$$E = E_{cm} + E_{int} \tag{3.8}$$

Hence, the internal and translational motions can be completely separated from each other. $\hat{T}_{cm}$ is defined as:

$$\hat{T}_{CM} = -\frac{\hbar^2}{2m}\nabla_{cm}^2 \tag{3.9}$$

Therefore, from Equation 3.6:

$$\phi_{cm} = e^{ik.R_0} \tag{3.10}$$

$R_0(X_0, Y_0, Z_0)$ is the position vector of the molecular centre of mass. The classical translational momentum is defined by:

$$P_{cm} = \hbar k \tag{3.11}$$

$$E_{cm} = \frac{P^2}{2m} \tag{3.12}$$

$$k^2 = \frac{2mE_{cm}}{\hbar^2} \tag{3.13}$$

The translational operation ($\hat{R}_T$) does not have any influence on the ϕ_{int}:

$$\begin{gathered} R_T = e^{i\boldsymbol{k}.A} \\ R_T e^{i\boldsymbol{k}.R_0} = e^{i\boldsymbol{k}.(R_0+A)} \end{gathered} \tag{3.14}$$

$$\begin{gathered} R_T\phi = R_T\phi_{int}\phi_{cm} = \phi_{int}R_T\,\phi_{cm} = \phi_{int}R_T e^{i\boldsymbol{k}.R_0} = \phi_{int}\ e^{i\boldsymbol{k}.(R_0+A)} = \\ \phi_{int}\ e^{i\boldsymbol{k}.A}\ \phi_{cm} \end{gathered} \tag{3.15}$$

The translational operation is determined with the $\boldsymbol{k}$ vector; therefore, the translational motion is neglected; and, the focus is on the complete internal motion (rotational and vibrational motion).

3.2 Principal Moments of Inertia

Rotational motion of objects is associated with their moment of inertia. Inertial moment of a rigid body in three dimensions is shown by a 3×3 matrix:

$$[I] = \begin{bmatrix} I_{xx} & I_{xy} & I_{xz} \\ I_{yx} & I_{yy} & I_{yz} \\ I_{zx} & I_{zy} & I_{zz} \end{bmatrix} \tag{3.16}$$

where for the systems of *n* particles:

$$I_{ii} = \sum_n m_n (j_n^2 + k_n^2) \quad ; \quad \text{For } i,j,k \in \{x,y,z\} \tag{3.17}$$

$$I_{ij} = -\sum_n m_n i_n j_n \quad ; \quad \text{For } i \neq j \in \{x,y,z\} \tag{3.18}$$

If the above tensor is diagonalized, the diagonal elements are called the principal moments of inertia and the related axes are called the principal moments of inertia axes. These axes are symbolized by a, b and c and the corresponding moments of inertia are I_a, I_b and I_c. In this representation, the largest and smallest moments of inertia belong to the c and a axes, respectively. It means that they always satisfy the relationship:

$$I_a \leq I_b \leq I_c \tag{3.19}$$

The rotational constants are defined based on the principal moment of inertia with the unit of Joules:

$$A= \frac{\hbar^2}{2I_a} \qquad B= \frac{\hbar^2}{2I_b} \qquad C= \frac{\hbar^2}{2I_c} \tag{3.20}$$

Using the rotational constants, the rotational Hamiltonian can be written as:

$$\hbar^2 \widehat{H}_{rot}=A\hat{J}_a^2 + B\hat{J}_b^2 + C\hat{J}_c^2 \tag{3.21}$$

Different molecular structures, such as linear, prolate, oblate, spherical top and asymmetric top, can be determined in terms of the relationship among their moments of inertia (Table 3.1).

Table 3.1: Relationships between the moments of inertia and molecular structures

Structure	Moments of inertia	Example
Linear	$I_b=I_c$, $I_a=0$	Acetylene (C_2H_2)
Prolate	$I_a<I_b=I_c$	Methyl chloride (CH_3Cl)
Oblate	$I_a=I_b<I_c$	Boron trifluoride (BF_3)
Spherical Top	$I_a=I_b=I_c$	Carbon tetrachloride (CCl_4)
Asymmetric Top	$I_a<I_b<I_c$	Nitrogen dioxide (NO_2)

The planar $N_2O – (C_2H_2)_2$ cluster that is of interest in this thesis is an asymmetric top; thus its moments of inertia are all distinct.

There are six different methods of mapping the principal moments of inertia axes. In this thesis, the first mapping (I^r), as presented in Table 3.2, has been used. I^r and III^r representations are adopted to calculate prolate top and oblate top wavefunctions respectively (See Section 3.4).

Table 3.02: Six methods of mapping the principle axes, subscript *r* and *l* refer to the right and left handed coordinate systems

	I^r	II^r	III^r	I^l	II^l	III^l
X	b	c	a	c	a	b
Y	c	a	b	b	c	a
Z	a	b	c	a	b	c

3.3 Euler Angles and Angular Momentum

To explain the reason for the necessity of using Euler angles, different coordinate systems in which Hamiltonian can be written, should be discussed. A general molecular Hamiltonian should be written in a frame that includes both the origin and the orientation of its axes fixed in space. This frame is called laboratory-fixed frame and is used to describe the three-dimensional (3D) motions (translational, rotational and vibrational) of a molecule. Writing a non-rotating Hamiltonian in a new frame, the origin of which is at the centre of the mass and the axis of which is parallel to the laboratory-fixed frame, can separate the translational Hamiltonian part from the rotational and vibrational Hamiltonian parts.

In this new frame, the rotational and vibrational Hamiltonians are invariant; therefore their eigenvalues stay the same. This frame is called the space-fixed or (X, Y, Z) frame. Using the molecule-fixed or (x, y, z) frame separates the Hamiltonian into vibrational and rotational parts in the lowest order. The origin of this frame is at the centre of the mass of the molecule, and its axes are defined by Euler angles (α, β, γ). This frame defines the instantaneous orientation of bonds and atoms with respect to the space-fixed frames. This transformation between the space-fixed frame and molecule-fixed frame is carried out using the Euler angles involving three successive rotations (Figure 3.1):

a) The (X, Y, Z) coordinate should be rotated by β about the Z axis to get (X', N, Z),

b) Rotating (X', N , Z) by α about the N axis leads to (X'', N, z), and

c) Rotating (X'', N, z) by γ about the z axis gets (x, y, z).

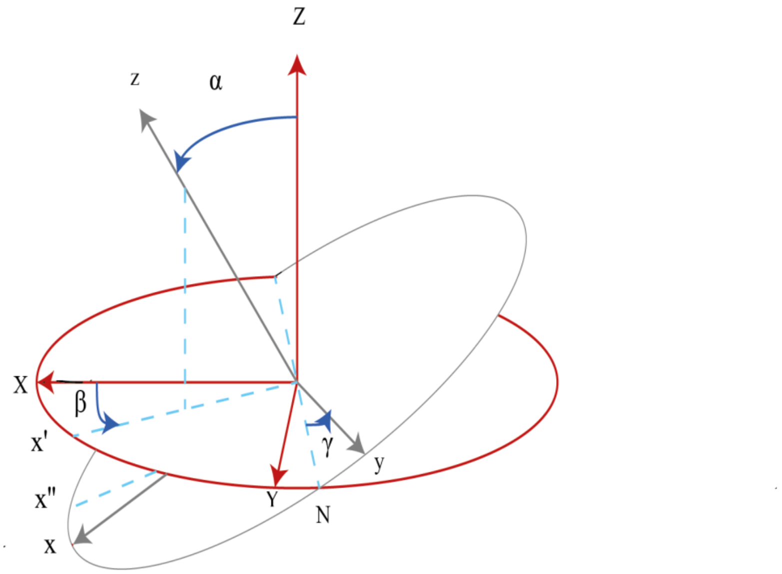

Figure 3.1: Euler angles in I^r representation

The angles are constrained to $0 \leq \alpha \leq \pi$, $0 \leq \beta \leq 2\pi$ and $0 \leq \gamma \leq 2\pi$. These two coordinate systems are related to each other by the matrix transformations of:

$$\begin{bmatrix}x\\y\\z\end{bmatrix} = R(\beta)R(\alpha)R(\gamma)\begin{bmatrix}X\\Y\\Z\end{bmatrix} = \begin{bmatrix}a_{11} & a_{12} & a_{13}\\ a_{21} & a_{22} & a_{23}\\ a_{31} & a_{32} & a_{33}\end{bmatrix}\begin{bmatrix}X\\Y\\Z\end{bmatrix} \qquad (3.22)$$

$R(\alpha)$, $R(\beta)$ and $R(\gamma)$ are the rotation matrixes and defined as:

$$R(\alpha) = \begin{bmatrix}cos\alpha & 0 & -sin\alpha\\ 0 & 1 & 0\\ sin\alpha & 0 & cos\alpha\end{bmatrix}$$

$$R(\beta) = \begin{bmatrix}cos\beta & sin\beta & 0\\ -sin\beta & cos\beta & 0\\ 0 & 0 & 1\end{bmatrix} \qquad (3.23)$$

$$R(\gamma) = \begin{bmatrix}cos\gamma & sin\gamma & 0\\ -sin\gamma & cos\gamma & 0\\ 0 & 0 & 1\end{bmatrix}$$

Based on the above definition, the angular momentum transformation is:

$$\begin{bmatrix} J_x \\ J_y \\ J_z \end{bmatrix} = R(\beta)R(\alpha)R(\gamma)\begin{bmatrix} J_X \\ J_Y \\ J_x \end{bmatrix} \tag{3.24}$$

Introducing $J_p = -i\,\hbar \frac{\partial}{\partial p}$ with $p = \alpha, \beta, \gamma$, the angular momentum about (x, y, z) can be written as:

$$\begin{aligned} \hat{J}_x &= sin\gamma\hat{J}_\alpha - csc\alpha cos\gamma\hat{J}_\beta + cot\alpha cos\gamma\hat{J}_\gamma \\ \hat{J}_y &= cos\gamma\hat{J}_\alpha + csc\alpha sin\gamma\hat{J}_\beta - cot\alpha sin\gamma\hat{J}_\gamma \\ \hat{J}_z &= \hat{J}_\gamma \end{aligned} \tag{3.25}$$

Then,

$$\begin{aligned} \hat{J}_X &= -sin\beta\hat{J}_\alpha + csc\alpha cos\beta\hat{J}_\gamma - cot\alpha cos\beta\,\hat{J}_\beta \\ \hat{J}_Y &= cos\beta\hat{J}_\alpha + csc\alpha sin\beta\hat{J}_\gamma - cot\alpha sin\beta\hat{J}_\beta \\ \hat{J}_Z &= \hat{J}_\beta \end{aligned} \tag{3.26}$$

In each frame, the magnitude of angular momentum remains constant:

$$\hat{J}^2 = \hat{J}_x^2 + \hat{J}_y^2 + \hat{J}_z^2 = \hat{J}_X^2 + \hat{J}_Y^2 + \hat{J}_Z^2 \tag{3.27}$$

Considering the above equations, one can show that:

$$[\hat{J}_i, \hat{J}_j] = i\hbar \sum_k \epsilon_{ijk} J_k \qquad and \quad i, j, k \in \{X, Y, Z\} \tag{3.28}$$

$$[\hat{J}_p, \hat{J}_q] = -i\hbar \sum_n \epsilon_{pqr} J_r \quad and \quad p, q, r \in \{x, y, z\} \tag{3.29}$$

$$\epsilon_{abc} = \begin{cases} +1 & \text{for even permutation of } a, b, c \\ 0 & \text{otherwise} \\ -1 & \text{for odd permutation of } a, b, c \end{cases} \tag{3.30}$$

Each component of the total angular momentum in space-fixed frame commutes with any component in molecule-fixed frame; and, both of them commute with the square of the total angular momentum.

$$[\hat{J}_i, \hat{J}_p] = 0 \qquad [\hat{J}^2, \hat{J}_p] = 0 \qquad [\hat{J}^2, \hat{J}_i] = 0 \tag{3.31}$$

It can also be shown that:

$$[\hat{H}_{rot}, \hat{J}_Z] = 0 \qquad [\hat{H}_{rot}, \hat{J}^2] = 0 \tag{3.32}$$

$$[\hat{H}_{rot}, \hat{J}_z] = -i\hbar\left(\frac{1}{2I_x} - \frac{1}{2I_y}\right)(\hat{J}_x\hat{J}_y + \hat{J}_y\hat{J}_x) \tag{3.33}$$

$\hat{H}_{rot}$, $\hat{J}_Z$, $\hat{J}_z$ and J^2 have common eigenfunctions, which in I^r can be written as:

$$\hat{H}_{rot}|J, K_a, m\rangle = E|J, K_a, m\rangle \tag{3.34}$$

$$\hat{J}^2|J, K_a, m\rangle = \hbar^2 J(J+1)|J, K_a, m\rangle \qquad J = 0, 1, 2, \ldots \tag{3.35}$$

$$\hat{J}_z|J, K_a, m >= \hbar K_a|J, K_a, m > \qquad K_a = 0, \pm 1, \ldots \pm J \tag{3.36}$$

$$\hat{J}_Z|J, K_a, m >= \hbar m|J, K_a, m > \qquad m = 0, \pm 1, \ldots \pm J \tag{3.37}$$

In the above equations, m is the magnetic quantum number. Here, m is neglected because there is no external field.

3.4 Energy Levels for a Symmetric Top Structure

Considering equation 3.21 for the molecular rotational Hamiltonian and Table 3.1 for the relationships among principal moment of inertia, the rotational energy of the prolate and oblate symmetric top are written as:

$$\begin{aligned} E_p &= (A - B)K_a^2 + BJ(J+1) \\ E_o &= (C - B)K_c^2 + BJ(J+1) \end{aligned} \tag{3.38}$$

For $J \neq 0$, the energy of a prolate symmetric top increases with increasing K_a while the energy for an oblate top decreases when K_c is increased. Moreover, the energy levels with $K_a = 0$ or $K_c = 0$ are $(2J + 1)$-fold degenerate and those with $K_a \neq 0$ or $K_c \neq 0$ have $2(2J + 1)$-fold degeneracy.

In the case of spherical top symmetry (A=B=C), the rotational Hamiltonian is:

$$\hbar^2 \hat{H}_{rot} = B\hat{J}^2 \tag{3.39}$$

So, the energy for the spherical top is written as:

$$E_{sph} = BJ(J + 1) \tag{3.40}$$

Thus, each rotational state has (2*J*+1)-fold degeneracy due to K and $(2J + 1)$-fold degeneracy due to *m*, resulting in an overall degeneracy of $(2J + 1)^2$.

3.5 Energy Levels for an Asymmetric Top Structure

A ladder operator is known as either a raising or a lowering operator. If operators $\hat{A}$ and $\hat{B}$ are considered such that $\hat{A}|a\rangle = a|a\rangle$ and [$\hat{A}$, $\hat{B}$] =$b\hat{B}$, then $\hat{B}|a\rangle$ is an eigenfunction of $\hat{A}$ with the eigenvalue of a+b. Thus, it changes each eigenfunction of $\hat{A}$ to a new one, and the eigenvalues are laddered up or down depending on the value of b. Therefore, operator $\hat{B}$ is a ladder operator for the eigenfunctions of operator $\hat{A}$. The angular momentum ladder operators are written as:

$$J^{\pm} = \hat{J}_x \pm i\hat{J}_y \tag{3.41}$$

In the molecular fixed frame $\hat{J}_m^{\pm}$ is the ladder operator.

$$[\hat{J}^2, \hat{J}_m^{\pm}] = 0$$
$$[\hat{J}_z, \hat{J}_m^{\pm}] = [\hat{J}_x, \hat{J}_z] \pm i[\hat{J}_y, \hat{J}_z] = -i\hbar(-\hat{J}_y \pm i\hat{J}_x) = \mp\hbar\hat{J}_m^{\pm} \tag{3.42}$$

The same relationships can be written with $J_s^{\pm}$, which is the angular momentum in space fixed frame. The equations below are written in the molecular fixed frame:

$$\hat{J}_m^{\pm}|J, K_a, m\rangle = \hbar\sqrt{J(J+1) - K_a(K_a \mp 1)}\,|J, K_a \mp 1, m\rangle \tag{3.43}$$

$$\hat{J}_m^{\pm\,2}|J, K_a, m\rangle = \hbar^2\sqrt{J(J+1) - K_a(K_a \mp 1)}\sqrt{J(J+1) - (K_a \mp 1)(K_a \mp 2)}\,|J, K_a \mp 2, m\rangle \tag{3.44}$$

As previously discussed, for the asymmetric top, $I_a \neq I_b \neq I_c$. The rotational Hamiltonian is given by Equations 3.20 can be rewritten in terms of the angular momentum:

$$\hat{H}_{rot} = \frac{\hat{J}_a^2}{2I_a} + \frac{\hat{J}_b^2}{2I_b} + \frac{\hat{J}_c^2}{2I_c} \tag{3.45}$$

Since

$$\hat{J}^2 = \hat{J}_x^2 + \hat{J}_y^2 + \hat{J}_z^2 \tag{3.46}$$

Using Equation 3.35:

$$\hbar^2\hat{H}_{rot} = A\hat{J}_a^2 + B\hat{J}_b^2 + C\hat{J}_c^2 = \left(\frac{A+B}{2}\right)\left(\hat{J}_z^2 + \hat{J}_x^2\right) + C\hat{J}_y^2 + \left(\frac{A+B}{2}\right)\left(\hat{J}_z^2 - \hat{J}_x^2\right) = \left(\frac{B+C}{2}\right)\hat{J}^2 + \left(A - \frac{B+C}{2}\right)\hat{J}_z^2 + \left(\frac{B-C}{4}\right)\left(\hat{J}_m^{+\,2} + \hat{J}_m^{-\,2}\right) \tag{3.47}$$

Because $\hat{H}_{rot}$ is written for non-vanishing matrix elements both for the states with the same *J* and *m* and the states with the same K_a value or a K_a value that differs by two. The Hamiltonian matrix can be written as block diagonalized matrixes for each *J* value. Each block is made up of *2J+1* blocks for a given *m* value, due to the *2J+1*-fold degeneracy in *m*.

The Hamiltonian matrix can be block diagonalized further into four blocks by summing or subtracting $|J, K_a, m \ = \ 0\rangle$ and $|J, -K_a, m \ = \ 0\rangle$ eigenfunctions. The reason is that there is a non-zero element for the matrix $\langle J, K_a', 0 \left| \widehat{H}_{rot} \right| J, K_a, 0\rangle$, only when K_a and K'_a are both odd or even. The four blocks are then categorized as E^+, E^-, O^+ and O^-, depending on whether they are formed by + or − linear combinations of the symmetric top wavefunctions and whether K_a is even or odd. The matrix elements for J = 0, 1, 2 are discussed in the following paragraphs:

The Hamiltonian matrix for J = 0 is a 1 × 1 block with $|J = 0, K_a = 0, m \ = \ 0\rangle$. Based on Equation 3.44 and 3.35 to 3.37 this matrix element is zero.

$$E_{rot}(J = 0) = 0 \tag{3.48}$$

For the case of J = 1, the Hamiltonian matrix is a 3 × 3 matrix with $|J = 1, k_a = 1, m \ = \ 0\rangle$, with $|J = 1, K_a = 0, m \ = \ 0\rangle$and with $|J = 1, K = -1, m \ = \ 0\rangle$ symmetric top basis. Consequently, the matrix is given by:

$$\widehat{H} = \begin{array}{c} \\ \langle 1,1| \\ \langle 1,-1| \\ \langle 1,0| \end{array} \begin{array}{c} \begin{array}{ccc} |1,1\rangle & |1,-1\rangle & |1,0\rangle \end{array} \\ \begin{bmatrix} A + \frac{B+C}{2} & \frac{B-C}{2} & 0 \\ \frac{B-C}{2} & A + \frac{B-C}{2} & 0 \\ 0 & 0 & B + C \end{bmatrix} \end{array} \tag{3.49}$$

The previous matrix can be divided into two block, one 2 × 2 block and one 1 × 1 block. The asymmetric top wavefunctions can be rewritten in the basis of the symmetric top eigenfunctions:

$$\begin{gathered} |1,1, O^+\rangle = \frac{1}{\sqrt{2}}(|1,1\rangle + |1,-1\rangle) \\ |1,1, O^-\rangle = \frac{1}{\sqrt{2}}(|1,1\rangle - |1,-1\rangle) \\ |1,0, E^+\rangle = |1,0\rangle \end{gathered} \tag{3.50}$$

Thus,

$$\begin{array}{c|ccc} & |1,1,O^+\rangle & |1,1,O^-\rangle & |1,0,E^+\rangle \\ \hline \langle 1,1,O^+| & A+B & 0 & 0 \\ \langle 1,1,O^-| & 0 & A+C & 0 \\ \langle 1,0,E^+| & 0 & 0 & B+C \end{array} \qquad (3.51)$$

The energy levels for *J* = 1 are:

$$E_{rot}(1,1,O^+) = \mathrm{A} + \mathrm{B}$$

$$E_{rot}(1,1,O^-) = \mathrm{A} + \mathrm{C} \qquad (3.52)$$

$$E_{rot}(1,0,E^+) = \mathrm{B} + \mathrm{C}$$

The same procedure can be used for $J = 2,3,\ldots$. For $J = 2$, the Hamiltonian matrix is a 5×5 matrix with $|J = 2, K_a = \pm 2, m = 0\rangle$, $|J = 2, K_a = \pm 1, m = 0\rangle$ and $|J = 2, K_a = 0, m = 0\rangle$ symmetric top basis. The proper basis functions for calculating the energy levels of asymmetric top are:

$$|J = 2, K_a = \pm 2, E^\pm\rangle = \frac{(|2,2\,\rangle \pm |2,-2\,\rangle)}{\sqrt{2}}$$

$$|J = 2, K_a = 0, E^+\rangle = |2,0\,\rangle \qquad (3.53)$$

$$|J = 2, K_a = \pm 1, O^\pm\rangle = \frac{(|2,1\,\rangle \pm |2,-1\,\rangle)}{\sqrt{2}}$$

The Hamiltonian matrix can be written as:

$$\hat{H} =$$

$$\begin{array}{c} \langle 2,0,E^+| \\ \langle 2,2,E^+| \\ \langle 2,2,E^-| \\ \langle 2,1,O^+| \\ \langle 2,1,O^-| \end{array} \begin{bmatrix} 3(B+C) & \sqrt{3}(B-C) & 0 & 0 & 0 \\ \sqrt{3}(B-C) & 4A+B+C & 0 & 0 & 0 \\ 0 & 0 & 4A+B+C & 0 & 0 \\ 0 & 0 & 0 & A+4B+C & 0 \\ 0 & 0 & 0 & 0 & A+B+4C \end{bmatrix} \qquad (3.54)$$

As can be seen above, there are three 1×1 blocks and one 2×2 block. Therefore, there are five different energy levels for J = 2, as listed below:

$$
\begin{gathered}
E_{rot}(2,2,E^{+}) = 2(A+B+C) \pm \sqrt{3(B-C)^2 + (2A-B-C)^2} \\
E_{rot}(2,0,E^{+}) = 2(A+B+C) \pm \sqrt{3(B-C)^2 + (2A-B-C)^2} \\
E_{rot}(2,2,E^{-}) = 4A+B+C \\
E_{rot}(2,,1,O^{+}) = A+4B+C \\
E_{rot}(2,1,O^{-}) = A+B+4C
\end{gathered}
\tag{3.55}
$$

Labeling of the energy levels is completed by considering the correlation diagram that links the energy levels of an asymmetric top with those of a prolate and oblate top, but $I_a \le I_b \le I_c$ is required. Energy levels of oblate and prolate symmetric tops are given in equation 3.38 [38]. By the condition mentioned above $(I_a \le I_b \le I_c)$, $(A-B) > 0$ and $(C-B) < 0$. For a specific J, as the K_a increases, the energy levels of K_a increase for a prolate top; whereas, the energy levels of an oblate top decrease as K_c increases. In the correlation diagram, the energy levels are not to scale, and the lines connecting the prolate to oblate top levels correspond to a hypothetical distortion of a molecule from a prolate top to an oblate top.

One can connect the energy levels and the two limiting quantum numbers K_a and K_c by applying a non-crossing rule to tag each level. The asymmetric levels are labeled $J_{K_aK_c}$. However, K_a and K_c are tags for asymmetric top and turn into good quantum numbers only in prolate and oblate symmetric top limits (Figure 3.2).

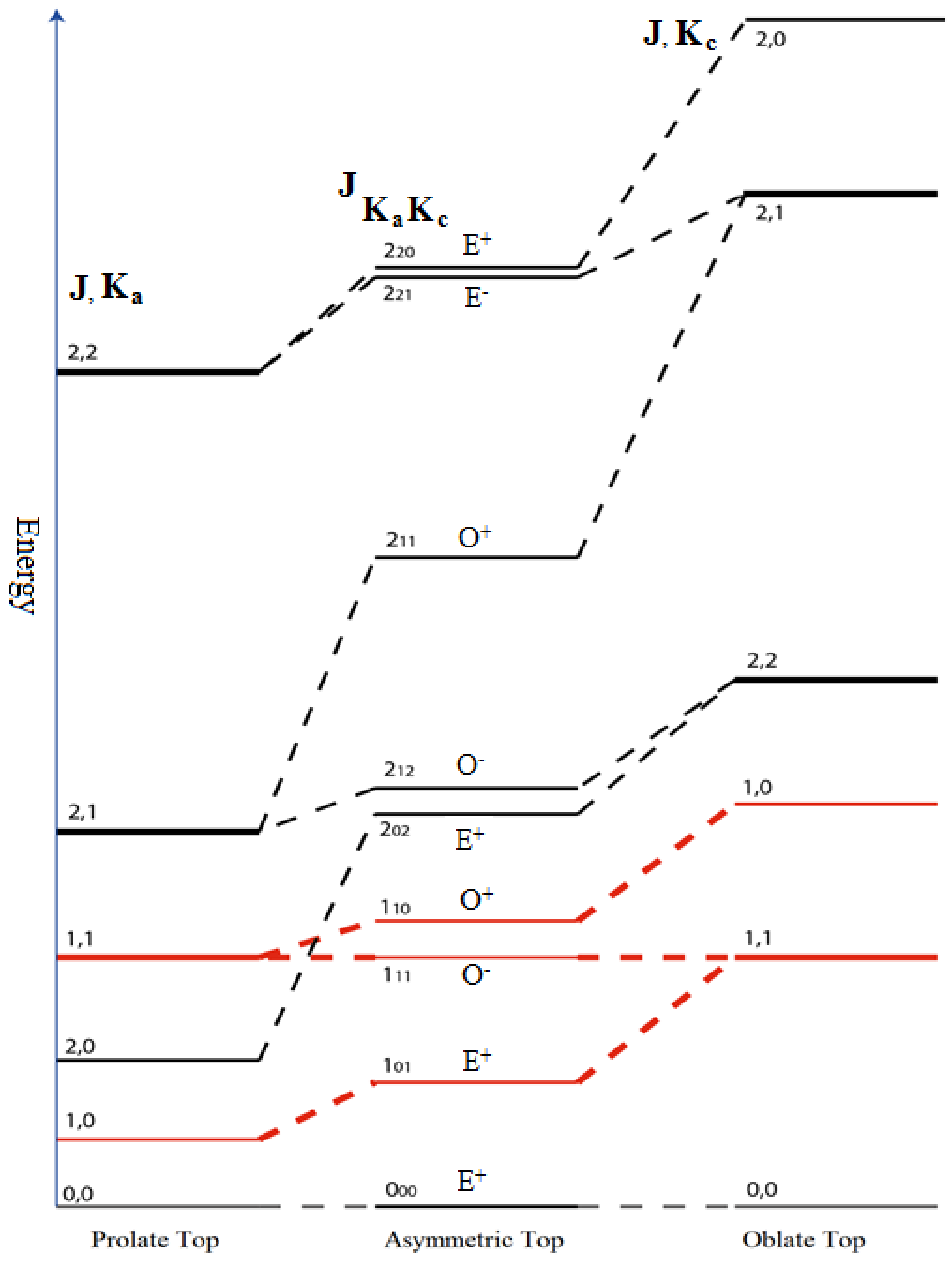

Figure 3.2: Prolate-oblate energy levels correlation diagram; For the right side (*A*,*B*,*C*) = (10,10,1), for the left side (*A*,*B*,*C*) = (10,1,1) and for the centre (*A*,*B*,*C*) = (10,5.5,1)

The sum of K_a and K_c would be equal to J or $J+1$. The difference between K_a and K_c has been labeled as $\tau = K_a - K_c$, and τ can be changed from $+J$ to $-J$ in order of descending energy. This label highlights that there are $2J+1$ different energy levels related to $2J+1$

different potential values for τ or K_a or K_c for every J. The expressions for energy levels for $J = 0, 1, 2$ of a rigid asymmetric rotor are given in Table 3.3.

Table 3.3: Energy levels of rigid asymmetric rotor for J = 0, 1, 2 (P.F.Bernath, 2005)

$J_{K_aK_c}$	J_τ	Energy Levels
0_{00}	0_0	0
1_{10}	1_1	$A + B$
1_{00}	1_0	$A + C$
1_{01}	1_{-1}	$B + C$
2_{11}	2_0	$A + 4B + C$
2_{12}	2_{-1}	$A + B + 4C$
2_{21}	2_1	$4A + B + C$
2_{02}	2_{-2}	$2(A + B + C) - \sqrt{3(B - C)^2 + (2A - B - C)^2}$
2_{20}	2_2	$2(A + B + C) + \sqrt{3(B - C)^2 + (2A - B - C)^2}$

Ray’s asymmetry parameter defines the degree of asymmetry and is denoted by κ. It can be varied from -1 for a prolate top (B = C) to +1 for an oblate top (A = B). It is written as [38]:

$$\kappa = \frac{(2B - A - C)}{A - C} \tag{3.56}$$

The theoretical rotational constants and Ray’s asymmetry parameter for the planar isomer of N_2O – $(C_2H_2)_2$ are given in Table 3.4, which are discussed in more detail in Chapter 5. In this table, the specific form of the difference between moments of inertia ($I_c - I_a - I_b$ inertial defect) is a positive small value, which represents a planar structure.

Table 3.4: Calculated rotational constants, asymmetry parameter and moments of inertia of planar isomer of N_2O – $(C_2H_2)_2$

A	3142.08 MHz
B	1075.03 MHz
C	800.98 MHz
κ	0.77
I_a	160.84 amu.Å^2
I_b	470.11 amu.Å^2
I_c	630.99 amu.Å^2
$I_c - I_a - I_b$	0.0003 amu.Å^2

3.6 Selection Rules

Generally speaking, any arbitrary object has three components of dipole moments – $\mu_a,\ \mu_b$ and μ_c – which are oriented along the principal axes. For a non-vanishing dipole moment, there is a specific set of selection rules that results in a group of transitions. The selection rules on v (vibrational quantum number), and J (total angular momentum quantum number) are $\Delta v = +1$ in absorption, $\Delta J = 0, \pm 1$, for vibrational fundamentals of the asymmetric tops. Transitions with $\Delta J = 0,\ \Delta J = +1$ and $\Delta J = -1$ are referred to the Q-branch, R-branch and P-branch, respectively.

***a*-type transitions** arise from non-zero component of the dipole moment along the *a* principal axis is not zero ($\mu_a \neq 0$). Then, $\Delta K_a = 0, (\pm 2, \pm 4, \dots)$ and $\Delta K_c = \pm 1, (\pm 3, \pm 5, \dots)$, with the transitions in parentheses being much weaker.

***b*-type transitions** arise from non-zero component of the dipole moment along the *b* principal axis is not zero ($\mu_b \neq 0$). Then, $\Delta K_a = \pm 1, (\pm 3, \pm 5, \dots)$ and $\Delta K_c = \pm 1, (\pm 3, \pm 5, \dots)$, with the transitions in parentheses being much weaker.

***c*-type transitions** arise from non-zero component of the dipole moment along the *c* principal axis is not zero ($\mu_c \neq 0$). Then, $\Delta K_a = \pm 1, (\pm 3, \pm 5, \dots)$ and $\Delta K_c = 0, (\pm 2, \pm 4, \dots)$, with the transitions in parentheses being much weaker.

An asymmetrical molecule can have all the three types of transitions, because $\mu_a \neq\ \mu_b \neq\ \mu_c \neq 0$.

3.7 Molecular Symmetry

This section deals with questions, such as what is molecular symmetry, and how symmetry can be used in the analysis of molecular spectra. It explains the Complete Nuclear Permutation (CNPI) Inversion and molecular symmetry group. Also, it discusses the molecular symmetry group, point group symmetry and character table.

Classifying molecules in terms of their symmetry elements is very important, because it can help to classify the energy levels of a molecule. The elements of the symmetry group of a molecule commute with the Hamiltonian of the molecule, so they do not change the energy of the molecule. This classification corresponds to the symmetry operations, with at least one common point remaining unaffected, and it leads to point groups that follow point group symmetry rules [39].

3.7.1 CNPI Group and Molecular Symmetry Group

Complete Nuclear Permutation Inversion (CNPI) group is the direct product of the all the possible permutations of identical nuclei in the molecule and the inversion group (i.e.$\varepsilon = \{E, E^*\}$). Each elements of the CNPI group commute with the Hamiltonian of the molecule in free space, thus this group is a symmetry group of the molecule [37].

The symmetry labels of the complete nuclear inversion group of a molecule can be used to label its energy levels. To find out the number of equilibrium versions it is essential to label the nuclei, then determine the number of versions of the equivalent structure by permuting the labels on the identical nuclei with and without inversion of the molecule to find as many as distinct forms as possible. For labeling the energy levels a subgroup of the CNPI group, which is called Molecular Symmetry (MS) group, is used. The elements of the MS group are obtained by removing the unfeasible elements of the CNPI group. An unfeasible element interconverts different equilibrium versions of the molecule which are separated by an impenetrable barrier in the potential energy surface; an impenetrable barrier does not allow observable tunneling to occur and does not involve bond breaking. The elements of the MS group commute with the internal Hamiltonian ($\widehat{H}_{int}$). As a result, the elements of the MS group can be used to label the rovibronic energy levels of the molecule [37].

3.7.2 Point Group Symmetry Operations

There are five different types of symmetry operations: identity, reflection, inversion, n-fold rotation and n-fold improper rotation. These operations are categorized as follows:

- $\boldsymbol{E}$ is the identity operator. It does nothing to the object. In other words, any object can experience this specific operation. Even very complicated molecules, such as DNA, can undergo this symmetry operation.
- $\boldsymbol{C_\mathrm{n}}$ is the rotation by an angle of around the n-fold symmetry axis. For example, C_6H_6 has six 2-fold axes, C_2 , and one 6-fold axis, C_6 (Figure 3.3).
- $\boldsymbol{\sigma}$ is a reflection in a mirror plane that may contain the highest symmetry axis of the molecule, which it is called vertical and represented by σ_v, or another axis perpendicular to the highest symmetry axis, which is called horizontal and denoted by σ_h. If a vertical mirror plane bisects the angle between two C_2 axes, it is called a dihedral plane and is denoted by σ_d . Related examples are H2O which has two vertical mirror planes and C_6H_6 that has six dihedral planes (Figure 3.3).

- $\boldsymbol{i}$ is the inversion operator through the centre of the mass of the molecule. Many molecules have a centre of inversion, such as C_6H_6.
- $\boldsymbol{S_n}$ is an improper rotation around the n-fold axis of symmetry and is a combination of two symmetry operations: A rotation followed by a reflection through a plane perpendicular to the axis of the rotation (Figure 3.3).

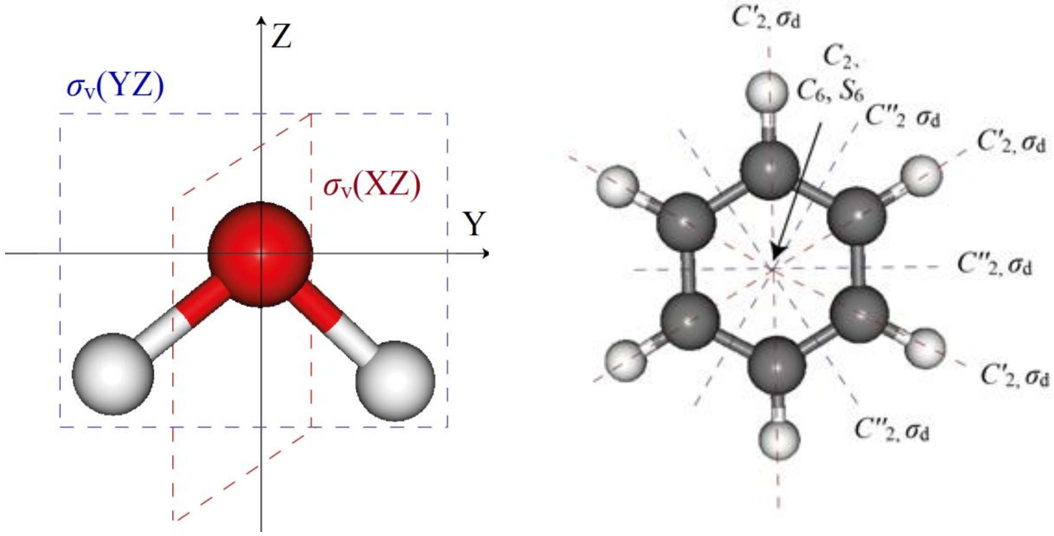

Figure 3.3: H_2O molecule with two vertical mirror planes (σ_v) YZ and XZ is shown on the left side of the figure. C_6H_6 molecule with six 2-fold axes (C_2), one 6-fold axis (C_6), six dihedral planes (σ_d) and one improper rotation (S_6) is shown on the right side of the figure. C_2' shows those symmetry axes that pass through C-H bonds and C_2'' shows those symmetry axes that bisect C-C bonds.

3.7.3 Symmetry Groups and Character Table of Planar N_2O – $(C_2H_2)_2$

The Schonflies notation describes 21 different kinds of point groups: $C_s(=C_{1h}=C_{1v}=S_1)$, $C_i(=S_2)$), C_n, D_n, C_{nv}, $C_{nh}(=S_n$ with n odd), D_{nh}, D_{nd}, S_n(with n even) , I, I_h, O, O_h, T, T_d and K_h [37]. These point groups are made up of point group symmetry operations, and any 3D object can have its place in one of these point groups. The related symmetry point group to the planar N_2O – $(C_2H_2)_2$ clusters is the C_s point group; therefore, only this point group is discussed in this thesis.

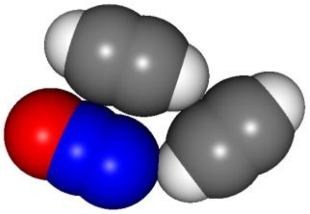

Figure 3.4: Theoretical structure for planar N_2O – $(C_2H_2)_2$ trimer with C_s symmetry

There are a few symmetry groups that can be applied when there are not any symmetry axes; one of these choices is the C_s point group. C_s point group has two symmetry elements. The first element is identity (E) and the second element is a mirror plane (σ).

3.7.4 Irreducible Representation and Character

The irreducible representation and character table are defined in this section. Consider matrix M which is rearranged to block-factored matrices M', M'', etc. as diagonal blocks and zero for the other elements, these block-factored matrices would be a reducible representation of this group. If these blocks cannot be changed further into block-factored matrices, then M', $M''$and etc. form an irreducible representations of the group; and, the sum of the traces of M', M'', etc. are the characters of this representation. The irreducible representations are called symmetry labels. Symmetry labels are used to determine the symmetry of the energy levels, nuclear spin statistical weights or the effect of adding external perturbation such as an electric or magnetic fields [37]. Table 3.5 is the character table for C_s point group.

Nuclear spin statistical weight is based on the Pauli Exclusion Principle. Bosons such as ^{12}C, ^{14}N, ^{16}O, and D have integer nuclear spins and fermions such as ^{15}N and H have half integer nuclear spins. According to Pauli Exclusion Principle two identical fermions cannot occupy the same identical energy state. The total wavefunction for two identical fermions has to be anti-symmetric with respect to the exchange of the two fermions. Determining the nuclear spin statistics and relative intensities depend on the existence of identical nuclei in the molecule that are exchanged by a symmetry element of the molecular point group. So, for a molecule without specific symmetry spin statistical weight has no effect on the population of energy levels [37]. Also, in the character table of C_s symmetry (Table 3.5), there is no permutation of bosons or fermions so there is no calculation of nuclear spin statistical weight and all of weights for rotational wavefunctions with even or odd J or K_a are 1. In addition, there is no discernable perturbation observed for this trimer.

Table 3.5: The $C_s(M)$ group character table [37]

	$\boldsymbol{E}$	$\boldsymbol{E}^*$
$C_s(M)$	1	1
C_s	E	σ_{ab}
Equivalent Rotation	R^0	R_c^π
A'	1	$1 : T_a, T_b, \hat{J}_c$
A''	1	$-1 : T_c, \hat{J}_a, \hat{J}_b$

3.7.5 Character Tables and Symmetry Classification of Rotational Wavefunctions

A character table consists of the characters of the irreducible representations of a group. All the elements in the same class have the same character in each irreducible representation and they can, therefore, be placed in one class (Two elements F and G in any group are in the same class if an element H exists such that $H^{-1}FH=G$). Although one element in each class is shown, the number of elements in each of class is pointed out (section 3.7.3). Every group has one irreducible representation for which all operations of the group have character $+1$. This is called the totally symmetric representation and in the C_s character table, it is denoted by A' [37].

In the C_s character table, the $C_s(M)$ is a notation for the molecular symmetry group of the planar N_2O – $(C_2H_2)_2$ in its ground electronic state. T_α is the translational coordinate. Changes in the Euler angles are represented by equivalent rotations, which are shown in the third row of Table 3.5. For symmetric top molecules, the notation R_z^β introduces a rotation by the angle β about the z axis **[**37**]**. R_π^α is the rotation of the molecule-fixed frame by α radians about an axis n in the xy plane that makes an angle of π with the x axis. Both α and β angles are measured in radians in a right-handed direction about the z axis. It is obvious from the character table that operator E and the rotation operator R^0 are equivalent to each other [37]. The transformation properties of symmetric top wavefunctions are [37]:

$$\begin{aligned} R_z^\beta |J,k,m\rangle &= e^{ik\beta}|J,k,m\rangle \\ R_\alpha^\pi |J,k,m\rangle &= (-1)^J e^{-2ik\alpha}|J,-k,m\rangle \end{aligned} \quad (3.57)$$

In Equation 3.57, m can be neglected due to the absence of any external fields. For asymmetric top molecules, notations R_a^π, R_b^π and R_c^π are used [37]. Here, the notation k is used instead of K ($K = |k|$). In the I^r representation, $R_c^\pi = R_{\frac{\pi}{2}}^\pi$ and $R^0 = R_z^0$ for the $C_s(M)$ point group. Using Equation 3.54 for $|J, K_a = 0, m\rangle$ basis:

$$\begin{aligned} R_z^0 |J,k_a = 0,m\rangle &= |J,k_a = 0,m\rangle \\ R_{\frac{\pi}{2}}^\pi |J,k_a = 0,m\rangle &= (-1)^J |J,k_a = 0,m\rangle \end{aligned} \quad (3.58)$$

For $|J, \pm k_a, m\rangle$;

$$R_z^0|J,\pm k_a,m\rangle = |J,\pm k_a,m\rangle$$
$$R_{\frac{\pi}{2}}^{\pi}|J,\pm k_a,m\rangle = (-1)^{J+k_a}|J,\mp k_a,m\rangle \tag{3.59}$$

In the III^r representation, $R^0 = R_z^0$ and $R_c^\pi = R_z^\pi$. Therefore, one can write Equations 3.55 and 3.56 in the basis of $|J,k_c = 0,m\rangle$ and $|J,\pm k_c,m\rangle$:

$$R_z^0|J,k_c = 0,m\rangle = |J,k_c = 0,m\rangle$$
$$R_z^\pi|J,k_c = 0,m\rangle = |J,k_c = 0,m\rangle \tag{3.60}$$

$$R_z^0|J,\pm k_c,m\rangle = |J,\pm k_c,m\rangle$$
$$R_z^\pi|J,\pm k_c,m\rangle = (-1)^{k_c}|J,\pm k_c,m\rangle \tag{3.61}$$

The characters produced by symmetric top wave functions are obtained from the trace of the rotation operators in matrix form in the basis of symmetric top wave functions. The rotation operators in matrix form in the basis of $|J,k_a = 0,m\rangle$ wave functions are:

$$tr(R_z^0) = [1] = 1$$
$$tr\left(R_{\frac{\pi}{2}}^{\pi}\right) = tr(R_c^\pi) = [(-1)^J] = (-1)^J \tag{3.62}$$

in the basis of $|J,\pm K_a,m\rangle$:

$$tr(R_z^0) = tr\begin{bmatrix}1 & 0\\0 & 1\end{bmatrix} = 2$$
$$tr\left(R_{\frac{\pi}{2}}^{\pi}\right) = tr(R_c^\pi) = tr\begin{bmatrix}0 & (-1)^{J+k_a}\\(-1)^{J+k_a} & 0\end{bmatrix} = 0 \tag{3.63}$$

The representations generated by prolate symmetric top wave functions $|J,k_a,m\rangle$ are presented in Table 3.6.

Table 3.6: Character representations generated by prolate symmetric top wavefunctions for $C_s(M)$ group

Equivalent Rotation	E R_z^0	E^* $R_{\frac{\pi}{2}}^{\pi}$
$\Gamma_{\lvert J,k_a=0,m\rangle}$	1	$(-1)^J$
$\Gamma_{\lvert J,\pm k_a,m\rangle}$	2	0

The rotation operators in matrix form in the basis of $|J, k_c = 0, m\rangle$ wave functions are:

$$tr(R_z^0) = tr[1] = 1$$
$$tr(R_c^\pi) = tr(R_z^\pi) = tr[1] = 1 \tag{3.64}$$

The characters of the above equations are 1 and 1, respectively.

In the basis of $|J, \pm k_c, m\rangle$:

$$tr(R_z^0) = tr\begin{bmatrix} 1 & 0 \\ 0 & 1 \end{bmatrix} = 2$$
$$tr\left(R^{\pi}_{\frac{\pi}{2}}\right) = tr(R_c^\pi) = tr\begin{bmatrix} (-1)^{k_c} & 0 \\ 0 & (-1)^{k_c} \end{bmatrix} = 2(-1)^{k_c} \tag{3.65}$$

The representations generated by oblate symmetric top wave functions $|J, K_c, m\rangle$ are presented in Table 3.7.

Table 3.7: Character representations generated by oblate symmetric top wavefunctions for $C_s(M)$ group

	E	E^*
Equivalent Rotation	R_z^0	R_z^π
$\Gamma_{\|J,K_c=0,m\rangle}$	*1*	*1*
$\Gamma_{\|J,\pm K_c,m\rangle}$	*2*	$2(-1)^{k_c}$

Considering Tables 3.1, 3.2 and 3.3, Table 3.8 shows the representation of the the $C_s(M)$ group for N_2O – $(C_2H_2)_2$ generated by basis functions $|J, k_a, m\rangle$ and $|J, k_c, m\rangle$.

Table 3.8: Representation of the $C_s(M)$ group generated by basis functions $|J, k_a, m\rangle$and $|J, k_c, m\rangle$

J	$\|k_a\|$	Γ_{rot}	J	$\|k_c\|$	Γ_{rot}
Odd	*0*	A''	J	*0*	A'
Even	*0*	A'	J	Odd	$2A''$
J	$\|k_a\|$	$A' + A''$	J	Even	$2A'$

The symmetry species of the asymmetric rotor wave functions can be determined by correlation of the K_a and K_c species labels given in Table 3.8. Figure 3.5 shows this correlation. Considering the correlation in Table 3.8 and Figure 3.5, Table 3.9 presents the related symmetry species.

Table 3.9: Symmetry species of $J_{K_aK_c}$ levels of $N_2O - (C_2H_2)_2$ in the $C_s(M)$ group

$J_{K_aK_c}$	Γ_{rot}
J_{ee}	A'
J_{eo}	A''
J_{oe}	A'
J_{oo}	A''

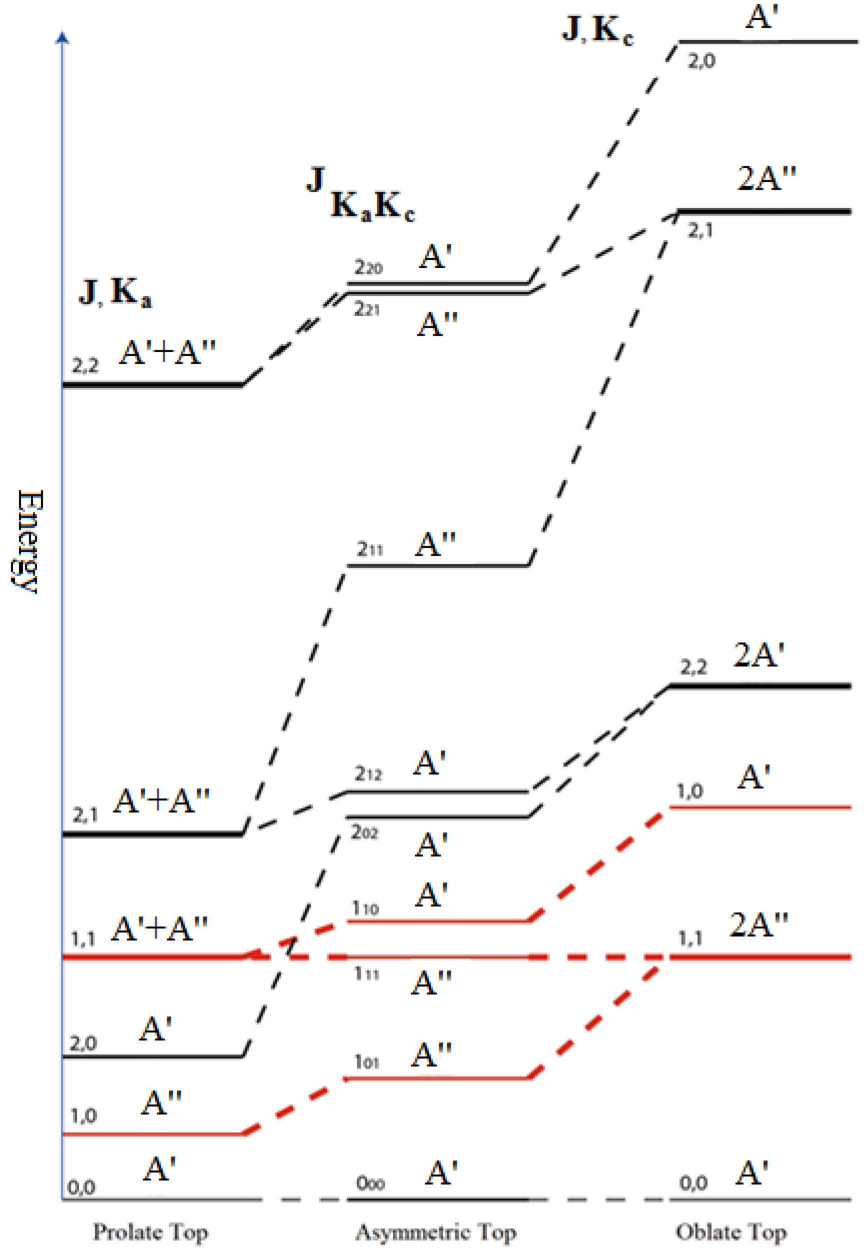

Figure 3.5: Correlation of asymmetric wavefunctions species with those of oblate and prolate symmetric top

3.8 Quantum Tunneling Effect

In the potential function of a molecule, there can be *n* versions of the global minimum at the equilibrium structures. The number of equilibrium structures is determined by labeling the nuclei of a molecule in its equilibrium structure and finding out the number of distinct version that can be obtained by permuting the labels on identical nuclei with or without inverting the molecule. To have distinct versions, the molecule should not be rotated but deformed across a potential barrier. If *n* versions of equilibrium structure (global minima) exist in the potential function of a molecule and a barrier between those states are high enough, then the wavefunction for each version localizes in its minimum position with no effective tunneling. So, each energy level will be n-fold structurally degenerate. Otherwise if the height of the barrier is low, tunneling occurs which lifts the degeneracy and the energy level is split [40]. In this section, the tunneling effect between different equilibrium structures is examined.

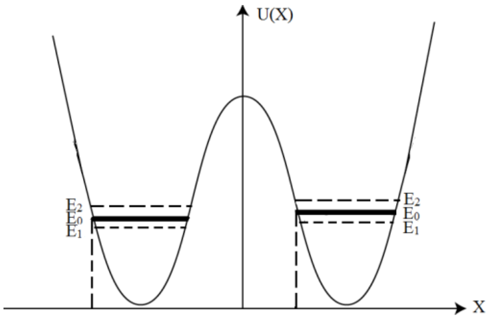

Figure 3.6: Field *U(x)* which is consisted of two potential wells. Tunneling occurs and E_0 is splitted into E_1 and E_2.

Considering the potential in Figure 3.5, the Hamiltonian can be written as:

$$\widehat{H}=\widehat{H}_1+\widehat{H}_2+\widehat{H}_T \tag{3.66}$$

where $\widehat{H}_1$ is the Hamiltonian of the particle on the left side of the barrier, $\widehat{H}_2$ is the Hamiltonian of the particle on the right side of the barrier, and $\widehat{H}_T$ is the Hamiltonian of the particle inside the barrier. The eigenvalues of $\widehat{H}_1$ and $\widehat{H}_2$ are defined as:

$$H_1\psi_l(a) = E_1\psi_l(a)$$

$$H_2\psi_r(a) = E_2\psi_r(a) \qquad (3.67)$$

where *l* is used for the left states and *r* for the right states.

The third term in Equation 3.63 shows the transfer between these states and the elements for the related matrix are defined by:

$$V_{lr} = \left\langle 1l \middle| \widehat{H}_T \middle| 2r \right\rangle \qquad (3.68)$$

Therefore, the Hamiltonian of Equation 3.63 can be formulated as:

$$\widehat{H}{=}\sum_{l\in 1} E_l|l\rangle\,\langle l| + \sum_{r\in 2} E_r|r\rangle\langle r| + \sum_{lr}[V_{lr}|l\rangle\langle r| + V_{lr}^{*}|l\rangle\langle r|] \qquad (3.69)$$

The eigenvectors of the Hamiltonian can be defined as:

$$|1\rangle = \begin{bmatrix}0\\1\end{bmatrix} \qquad |2\rangle = \begin{bmatrix}1\\0\end{bmatrix} \qquad (3.70)$$

If it is assumed that the potential is symmetric, then $E{=}E_1{=}E_2$ and the eigenstates are related to the diagonal Hamiltonian:

$$\widehat{H} = \begin{bmatrix}E & 0\\0 & E\end{bmatrix} \qquad (3.71)$$

With tunneling effect between these states with the characteristic matrix element V_{lr}, the Hamiltonian becomes:

$$\widehat{H} = \begin{bmatrix}E & V_{lr}\\V_{lr} & E\end{bmatrix} \qquad (3.72)$$

and the related eigenstates are:

$$\psi_e = \frac{1}{\sqrt{2}}\left(\begin{bmatrix}0\\1\end{bmatrix} + \begin{bmatrix}1\\0\end{bmatrix}\right)$$

$$\psi_o = \frac{1}{\sqrt{2}}(\begin{bmatrix}0\\1\end{bmatrix} - \begin{bmatrix}1\\0\end{bmatrix}) \qquad (3.73)$$

The energies of the above eigenstates are:

$$E_{e,o} = E \mp V \tag{3.74}$$

As it can be seen in the equation 3.74, the energy level is split into two energy levels with different energies. Therefore, the time-dependent solution is:

$$\begin{aligned} \psi(t) &= \begin{bmatrix} c_2 \\ c_1 \end{bmatrix} \\ &= \frac{c_e}{\sqrt{2}} \exp(-iE_e\, t) \begin{bmatrix} 1 \\ 1 \end{bmatrix} + \frac{c_o}{\sqrt{2}} \exp(-iE_o\, t) \begin{bmatrix} -1 \\ 1 \end{bmatrix} \end{aligned} \tag{3.75}$$

where c_e and $c_o$are the normalization constants.

From Equation 3.75, it can be concluded that the population between the left and right states oscillates with time. The probability of tunneling for a particle in the initial state of the system from the left side to the right side is described as:

$$P_{1\rightarrow 2} = |c_2|^2 = \frac{1}{2}(1 - \cos 2\alpha t) \tag{3.76}$$

where c_2 is the normalization constant. Thus, the tunneling probability has an oscillatory behaviour with time.

As we will see in the next section, the tunneling motion has been observed between the acetylene units in $(C_2H_2)_2$. Also, the barrier height was measured to be 33 cm^{-1} [48]. In the case of N_2O – $(C_2H_2)_2$ the spectral resolution was not sufficiently high to observe the splittings that may exist as a result of tunneling motion of the C_2H_2 dimer units. But failure to determine the precise geometrical structure of the trimer could be due to the existence of the tunneling motion between C_2H_2 monomers.

3.8.1 Inter-conversion Tunneling Motion in C_2H_2 Dimer

In 1977, Sakai et al. reported their findings on the intermolecular potential for acetylene [41]. Based on their semi-empirical calculations on potential energy surfaces, the lowest energy isomer of C_2H_2 dimer was found to be planar having C_{2h} symmetry [41]. Later in 1983, Pendley and Ewing performed Fourier Transform IR Spectroscopy on $(C_2H_2)_2$ and $(C_2D_2)_2$ [42]. They recorded several bands between 600 and 2800 cm^{-1} which represented the same result as Sakai et al.'s [42]. One year later, Miller et al. recorded 6 different bands (*A*-*F*) in the *CH* stretching region of C_2H_2 between 3200 and 3320 cm^{-1} [43]. They assigned those bands to dimer and larger clusters of acetylene [43]. Following Miller et al.'s experiment, Bryant et al. published their studies on bands *D* to *F* (3250-3300 cm^{-1}) of C_2H_2 dimer [44]. Their results show that the structure of the dimer is slipped parallel with C_{2h} symmetry while Prichard et al. observed and assigned band C to a nearly T-shaped structure [45].

There were efforts in determining the structure of acetylene dimer on the theoretical side, too. Aoyama, Matsuoka, and Nakagawa reported that the lowest energy isomer of the dimer has a T-shaped geometry [46]. The study by Alberts et al. confirmed the same structure for the lowest energy isomer and foundC_{2h} symmetry as a transition state [47]. These results were at odds with the semi-empirical calculations of Sakai et al.'s [42].

In 1988, Fraser et al. published a paper on the inter-conversion tunneling of the C_2H_2 dimer [48]. Their investigations revealed that this dimer has 4 minima on its potential energy surface and inter-conversion tunneling in C_2H_2 dimer splits the ground vibrational state into three tunneling states. A tunneling barrier of approximately 33 cm^{-1} corresponding to a tunneling rate of 2.2 GHz was reported (Figure 3.6) [48]. This tunneling motion causes the conversion of the

T-shaped structure with the lowest energy of the dimer to the parallel structure with higher energy and vice-versa (Figure 3.7).

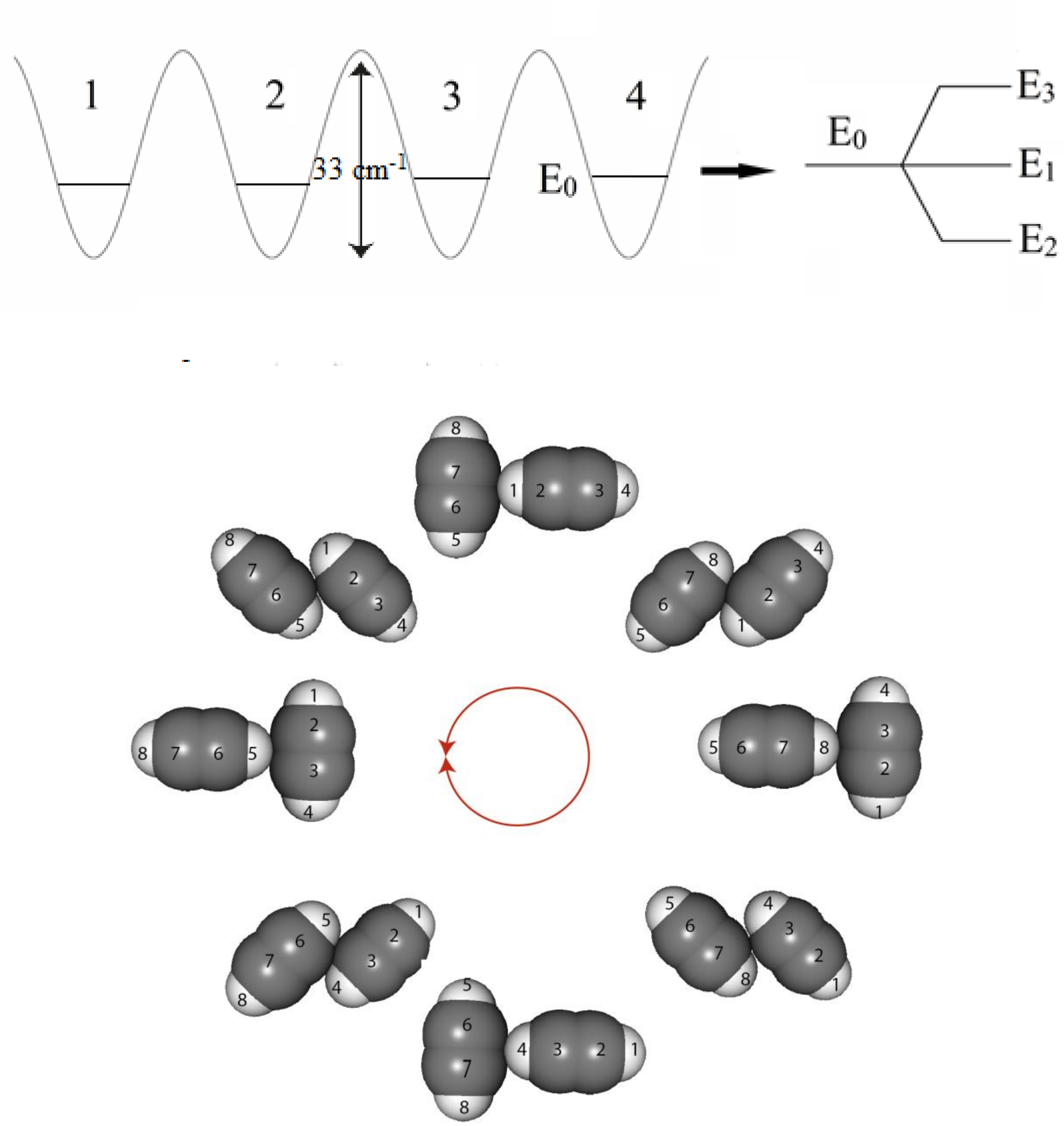

Figure 3.7: Inter-conversion tunneling for C_2H_2 dimer splits the ground vibrational state into three different states. The inter-conversion tunneling motion between T-shaped equilibrium structures of acetylene dimer is shown in this figure.

In 2000, Peebles and Kuczkowski reported the observation of a non-planar isomer of the OCS – $(C_2H_2)_2$ trimer [35]. Although they could perform semi-empirical calculations which predicted the trimer structure has two C_2H_2 monomers geometrically aligned between the T-shaped orientation [45] of the C_2H_2 dimer and a parallel shape, they could not precisely determine its structure. Their calculations showed that the observed non-planar isomer is not the lowest energy isomer. They concluded that the causes for the failure to determine the structure of the trimer might be related to the perturbation in the spectrum as a result of the existence of an inter-conversion tunneling motion, which gives a mirror image configuration [35] or the presence of another structure with a close energy to the first structure and the inter-conversion tunneling between the first and second structures, which would be mass sensitive [35]. In 2004, Valdes and Sordo performed semi-empirical calculations on OCS – $(C_2H_2)_2$. According to their studies, the geometrical structure of the trimer is an averaged structure between T-shaped and parallel structure of the acetylene dimer because of inter-conversion tunneling (See Section 2.5). [36].

The he possibility of inter-conversion tunneling effect in the monomers of C_2H_2 has been reported in other studies on the complexes containing the C_2H_2 dimer, such as the planar isomer of the OCS – $(C_2H_2)_2$ [18] and high-resolution spectroscopic studies on C_2H_2 and C_2D_2 van der Waals dimers [49, 50].

3.9 Harmonic Oscillator

$\widehat{H}_{rve}$ is separated into vibrational-rotational and electronic parts by Born-Oppenheimer approximation. As it is discussed in this chapter the rotational and vibrational parts of the Hamiltonian can be further separated from each other by changing the space-fixed frame to molecule-fixed frame. The rotational motion of molecules was explained in previous sections. The vibrational motion, in its simplest form, is modeled as a system of harmonic oscillators. A linear molecule with N nuclei has 3N-5 and a non-linear molecule has 3N-6 normal vibrational modes. Each of these modes can be considered as an independent harmonic oscillator.

The actual potential function for molecular vibrations may be anharmonic. The simple harmonic oscillator model provides a reasonable approximation of vibrational energy levels for small values of vibrational quantum number,v, where the anharmonicity effect is negligible.

Solving the Schrödinger equation for harmonic oscillator leads to the following equation for the vibrational energy:

$$E_v = \sum_{i=1}^{3N-6} (v_i + \frac{1}{2})\, h\omega_i \tag{3.77}$$

For the higher v where the anhormonicity is not negligible, higher order terms in the vibrational potential function are taken into account. For any two nuclei in molecules the potential can be modeled by a Morse potential (Figure 3.8), Lennard-Jones potential, etc. which allow occurring the anhormonicity in the potential. Also, they asymptotically approach a dissociation limit at large internuclear separation rather than having unlimited bound states in the harmonic oscillator model as v increases.

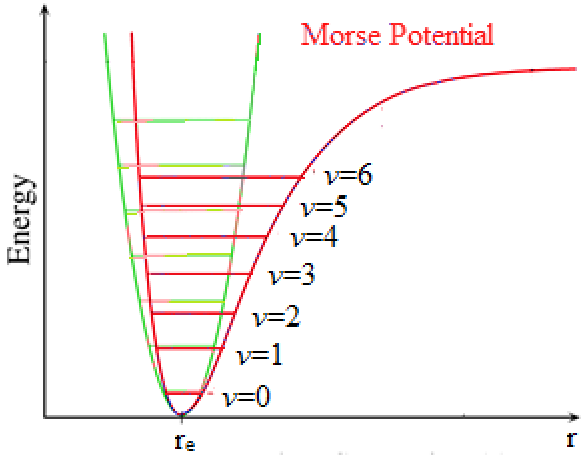

Figure 3.8: Comparing harmonic and Morse potential together

Morse potential is given by:

$$V_{vib}(r) = D(1 - e^{-a(r-r_e)})^2 \tag{3.78}$$

Here, D is the dissociation energy (well depth) and r_e is the distance between the nuclei at equilibrium and a controls the width of the potential. The vibrational energy levels for Morse potential can analytically be obtained.

$$E_v(v) = \omega_e \left(v + \frac{1}{2}\right) - \omega_e \chi_e (v + \frac{1}{2})^2 \tag{3.79}$$

Where χ_e anhormonic parameter, ω_e and $\omega_e \chi_e$ are defined in cm^{-1} as,

$$\begin{aligned} \omega_e &= a\sqrt{\frac{(10^2)hD}{2c\pi^2\mu}} \\ \omega_e \chi_e &= \frac{a^2 h(10^2)}{8\pi^2 \mu c} \end{aligned} \tag{3.80}$$

This vibrational motion determines the central frequency of the spectrum. Also, the vibrational motion of the molecule causes an average increase in bond-lengths of the molecule in the excited state, which leads to smaller rotational constants in comparison with those of the ground state.

3.10 Symmetry of Vibrational States

As discussed in section 3.8, molecules cannot be considered as a rigid rotor but atoms vibrate around their equilibrium positions in the molecule. Each molecule with N number of atoms has 3N total degrees of freedom out which 3 belong to translational motion of the centre of mass and 3 (non-linear molecular) or 2 (linear molecule) degrees of freedom are related to rotational motion. As a result, there are 3N-6 vibrational degrees of freedom available for non-linear molecules and there are 3N-5 vibrational degrees of freedom for linear molecules. Hence, N_2O – $(C_2H_2)_2$ has 3(11)-6=27 vibrational modes.

Using the point group symmetry of a molecule, one can determine the symmetry of the vibrational modes of that molecule. The C_s point group of the planar N_2O – $(C_2H_2)_2$ isomer contains one identity operation $(\hat{E})$ and one horizontal mirror plane operation $(\hat{\sigma})$ which includes all the atoms of the molecule. In this method, 3 displacement vectors are assigned to each atom. The transformation properties of the 3N displacement vectors are considered under all symmetry operations of the symmetry group of the molecule. So, The character of identity operation is 3N $(\chi^{3N}(\hat{E}) = 3N)$ which is the total character. Moreover, any $\hat{\sigma}$ contributes +1 for each atom to the total character since the trace of the reflection matrix is:

$$D = \begin{bmatrix} 1 & 0 & 0 \\ 0 & 1 & 0 \\ 0 & 0 & -1 \end{bmatrix} \tag{3.81}$$

The N_2O – $(C_2H_2)_2$ complex (N=11) has 33-dimensional reducible representation which can be reduced as [37]:

$$\Gamma^{3N} = \sum a_i \Gamma^i$$
$$a_i = \frac{1}{g}\sum_{\hat{R}} \chi^{3N}(\hat{R})\chi^i(\hat{R})^* \tag{3.82}$$

Where g represents the order of the group and sum runs over all the symmetry operations. Considering table 3.5, one can remove the symmetry species of translational motion and rotation from the total representation to find the vibrational modes [37]:

$$\Gamma^{vib.} = \Gamma^{3N} - \Gamma^{trans.} - \Gamma^{rot} \tag{3.83}$$

So, the reducible representation for the planar $N_2O - (C_2H_2)_2$ is:

$$a_{A'} = \frac{1}{2}(33 + 11) = 22$$

$$a_{A''} = \frac{1}{2}(33 - 11) = 11 \tag{3.84}$$

thus,

$$\Gamma^{33} = 22A' + 11A''$$

$$\Gamma^{trans.} = 2A' + A'' \tag{3.85}$$

$$\Gamma^{rot.} = A' + 2A''$$

using equation 3.83 the symmetry of the vibrational modes are:

$$\Gamma^{vib.} = 19A' + 8A'' \tag{3.86}$$

which results into 27 different vibrational modes for this trimer. Depending on which linear combination of coordinates are involved in the specific vibration modes it can have A'or A'' symmetry species.

Chapter 4: Experimental Setup

In this chapter, the theory of supersonic jet is presented and the application of this method is explained. The supersonic jet apparatus (supersonic jet combined with a laser in rapid scan mode) that was used in the investigation of $N_2O – (C_2H_2)_2$ is described. The basics of Quantum Cascade Laser (QCL) which was utilized in the apparatus for probing $N_2O – (C_2H_2)_2$ clusters are given followed by the demonstration of data acquisition method.

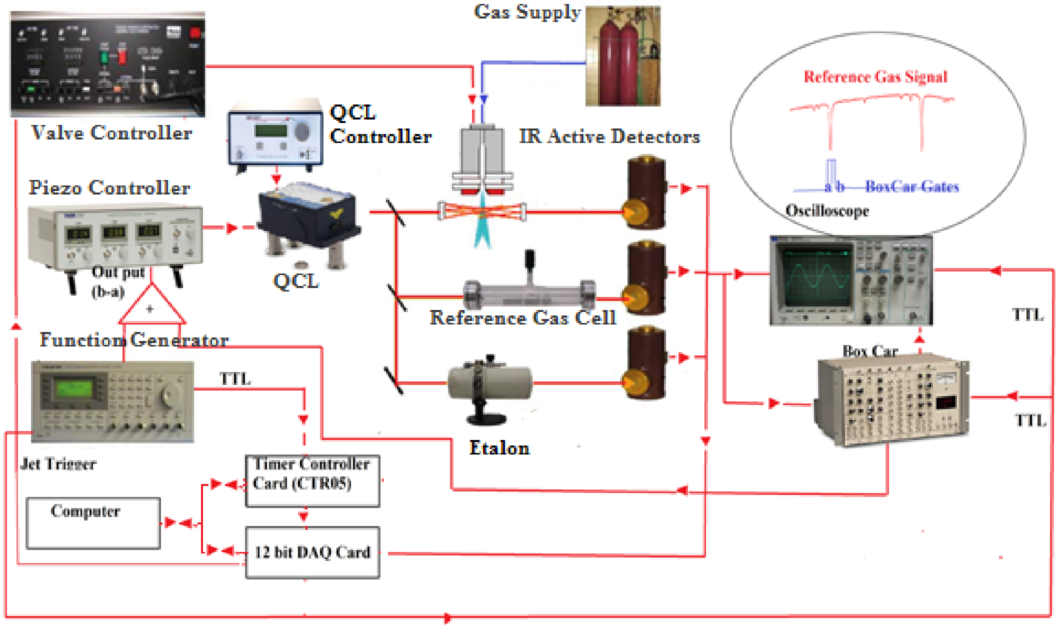

Figure 4.1: Schematic of the experimental setup which is discussed in sections 4.1-4.5.

Figure 4.1 is a schematic of the experimental setup which was used in the experiment. As it can be seen in the figure, spectra were recorded using a pulsed supersonic jet apparatus with the QCL. The system featured a multi-pass absorption cell in the jet chamber. Signals from a fixed etalon and a reference gas cell containing room-temperature N_2O were used for wavenumber calibration. The data acquisition procedure is further discussed in sections 4.3 and 4.4.

4.1 Theory and Application of Supersonic Jet in Spectroscopy

Very weakly bound van der Waals complexes with small dissociation energies can be generated and they become stable at low temperatures; since at high temperatures, kT is much larger than dissociation energy, these weakly bound complexes immediately dissociate, so the intermolecular forces cannot be examined. In order for weak intermolecular forces to dominate the thermal energy, the rotational temperature of the complexes' environment should be very low.

In a supersonic jet, the gas sample expands adiabatically from the gas chamber with high pressure through a nozzle into a vacuum chamber with low pressure; and, most of the initial thermal energy is converted into directed mass flow energy. This expansion occurs very quickly, so that no heat exchange occurs between the gas and environment. From conservation of energy, the total energy before and after the expansion can be written as:

$$U_0 + P_0V_0 + \frac{1}{2}mv_0^2 = U + PV + \frac{1}{2}mv^2 \qquad (4.1)$$

In Equation 4.1, for a mole of gas with mass m, the total internal energy is defined as $U = U_{trans} + U_{vib} + U_{rot}$, the potential energy after the expansion is PV and the kinetic energy after the expansion is $\frac{1}{2}mv^2$, in which v is the mean flow velocity of the expanding gas [51]. If the mass flow ($\frac{dm}{dt}$) is small through nozzles in comparison with the total mass of the gas in the reservoir, there is a thermal equilibrium inside the reservoir and, thus $v_0 = 0$. The gas pressure after the expansion is small $P \ll P_0$, as a result of the expansion in the vacuum chamber. Therefore, it is assumed that $P = 0$. Consequently, Equation 4.1 can be rewritten as:

$$U_0 + P_0V_0 = U + \frac{1}{2}mv^2 \tag{4.2}$$

When most of the initial energy, $U_0 + P_0V_0$, is converted into kinetic-flow energy, $\frac{1}{2}mv^2$, a cold molecular beam with small internal energy, U, may be obtained. The ratio of the velocity of flow to the speed of sound in such environment (jet) is called Mach (M) number. The speed of sound in a gas at temperature T is:

$$c_{sound} = \sqrt{\gamma RT} \qquad (4.3)$$

where R is the gas constant per unit mass and γ is $\frac{C_p}{C_v}$ where C_p and C_v are the specific heat capacities at constant pressure and volume, respectively. A high Mach number occurs due to the reduction in the temperature caused by expansion, which reduces the speed of sound in the jet [52].

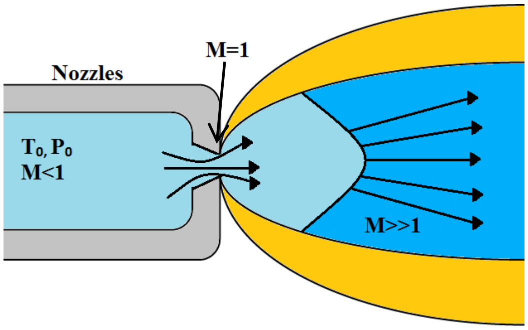

Figure 4.2: The small Mach number before the expansion and large Mach number after the expansion are shown in the figure and arrows show the flow of gas.

A supersonic beam is produced when the flow velocity, exceeds the local velocity of sound (Figure 4.2). A decrease in the internal energy results in a decrease in the relative velocities of the molecules, i.e. during the expansion, the faster molecules collide with slower ones and transfer kinetic energy (Figure 4.3). The collisions with the impact parameter zero narrow the velocity distribution of velocity component $v_{||} = v_z$ parallel to the flow direction z which results in a Maxwellian distribution around v_z corresponding to the translational temperature $T_{||}$ (Figure 4.3) [51].

From the macroscopic point of view, as a result of these collisions, the translational, rotational and vibrational temperatures decrease. The translational temperature is proportional to the width of the velocity distribution, whereas the vibrational and rotational temperatures can be determined from the intensity of rotational-vibrational transitions. The amount of the transferred energy reduces with decreasing relative velocity and density [51].

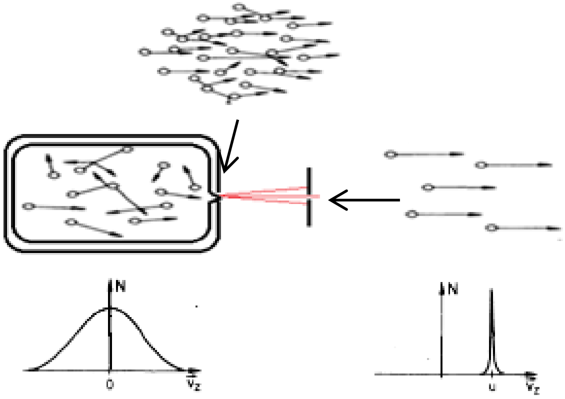

Figure 4.3: Velocity distribution before and after the expansion in the jet (Velocities of molecules are shown by vectors.)

Generally, the cross section for the transfer of energy in elastic collisions, $U_{trans} \rightarrow U_{trans}$, is larger than those of $U_{rot} \rightarrow U_{trans}$; therefore, the rotational energy of the molecules at the early stage in the expansion cannot be completely converted into flow energy during the short time interval of the expansion [51]. This means that the translational energy cools much faster than the rotational energy, $T_{trans} < T_{rot}$, or after the expansion, $U_{rot} > U_{trans}$. Cross sections for translational-vibrational energy transfer are even smaller than those of translational-rotational energy transfers; therefore, cooling of the vibrational energy is less effective [51]:

$$T_{trans} < T_{rot} < T_{vib} \tag{4.4}$$

An advantage of low vibrational and rotational temperatures is that the spectrum is noticeably simplified, because only the lowest rovibrational levels are populated in the ground electronic state: the decrease in spectral line congestion is helpful in the investigation of molecular clusters properties such as intermolecular forces and geometrical structure [52]. The most significant benefit of using supersonic jet expansion is that the species of interest travel in a collision free environment (removal of pressure broadening) with a narrow velocity distribution (a large decrease in Doppler broadening) [15].

4.2 Quantum Cascade Lasers

Utilization of QCLs as light sources for modern methods of spectroscopy in the mid- IR (4000–400 cm^{-1} or 2.5–25 μm), is growing rapidly. In comparison with diode lasers, which provide powers of about 1mW, QCLs offer power of up to 5 W that improve the intensity of the absorption signal [53], so the signal to noise of the spectrum is improved.

QCLs use epitaxially grown quantum wells that have electrons in lasing states. These types of lasers were first demonstrated by Bell Labs Team in 1994 [54]. The difference between QCLs and diode lasers is the design of the active region. In a QCL, the lasing transition occurs between states within a given quantum well; whereas, in a diode laser transitions arise between the conduction band and the valence band of the semiconductor material [55].

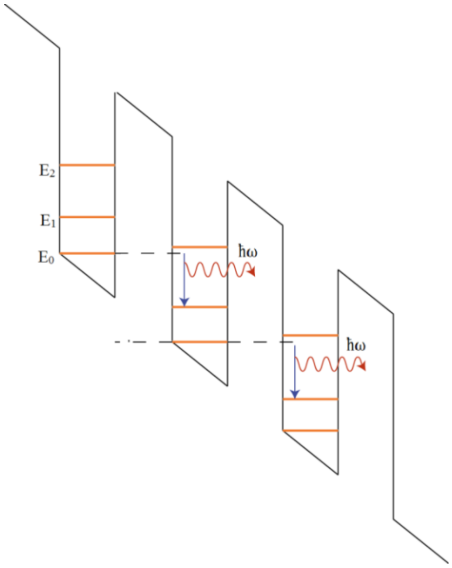

Figure 4.4: Cascade process: The red arrow shows the emitted photon as a result of the intersubband transition of the electron in the blue arrow. As it can be seen in the figure, the electron transition between ground state of the first quantum well to the excited state of the next quantum well should occur by tunneling through the barrier. Then the electron tunnels through the next quantum well and the whole process is repeated [56].

The benefit of the QCL structure is that the electron that is responsible for the emission of the photon tunnels into the next quantum well. Thus, multiple photons can be produced by a single electron. This specific feature allows QCLs to be very efficient. The tunneling from one well to the next one is called a quantum cascade process (Figure 4.4). The well depths can be changed by changing the layer depths in the fabrication procedure; hence, the wavelength of the lasing transition depends on the physical structure of the device. With careful design of the quantum wells, a QCL can lase with different wavelengths – as short as 2.75 µm [56, 57] or as long as 161 µm (1.9 THz) [58]. In order to achieve a longer wavelength, cryogenic cooling must be used: at room temperature, the observed wavelength is at most 16 µm [59]. The QCL which was used in the observation of a planar isomer of N_2O – $(C_2H_2)_2$, had a maximum power of 120 mW with a wavelength of around 4.5 µm at room temperature. This laser was operated at a temperature of about 19±5°C which was monitored by a Daylight Solution QCL controller.

4.3 Supersonic Jet Apparatus

The use of a diode laser in a rapid scan mode combined with a supersonic apparatus was first demonstrated by Rochat et al. [60] and later by A. R. W Mckellar's research group [61]. The rapid scan mode increases the signal to noise ratio by smoothing high frequency noise from the laser. Using this apparatus and signal averaging with continuous background subtraction result in a dramatic increase in the signal to noise ratio of the observed spectrum. The apparatus that was used in our study of $N_2O - (C_2H_2)_2$ is very similar to that used in reference [60, 61] except that a QCL instead of a diode laser was used as a source of radiation.

4.3.1 Supersonic Jet Apparatus and Vacuum System

Figure 4.5 shows the vacuum chamber that was used in our experiments. A NW250 six-way cross was attached to a gate valve; and, this valve was mounted on a Varian VHS-10 diffusion pump, which was backed by an Edwards E2M275 mechanical pump.

Figure 4.5: Six-way cross attached to a large diffusion pump

The background pressure of the vacuum chamber was monitored by an Edwards Active Inverted Magnetron Gauge. This pressure was on the order of 10^{-7} Torr, but could reach as high as 10^{-4} Torr during jet operation. The average flow of the gas was monitored by an ordinary thermocouple vacuum gauge.

In the apparatus, the gas mixture was pulsed into the vacuum chamber by two General Valve Series 9 pulsed nozzles, manufactured by Parker Hannifin Corporation. These valves are capable of operating up to a backing pressure of 85 atmospheres (1249 psi) and high repetition rates up to 125 Hz. The valve controller unit allows for pulse duration to be adjusted within the range of microseconds, milliseconds, seconds or minutes. In our experiments, the backing pressure was 140 psi, the pulse duration was 2.5 ms and the repetition was 1 Hz. The nozzles hung from a manifold connected to a quarter- inch gas supply tube, directly above the throat of the diffusion pump for efficient generation of molecular clusters.

4.3.2 Optical Setup

The optical setup is shown in Figure 4.6. In this setup the radiation of the QCL was directed through the optical setup using two gold-coated flat mirrors. Subsequently, there was a beam splitting step in which light was divided into two portions with relative intensities of about 0.8 to 0.2. The stronger part was focused at the centre of the jet chamber to probe the jet expansion. Another 45:55 beam splitter was used to divide the weaker part of beam into two parts. One part of the beams was directed into a passive etalon, and the other was directed into a reference gas cell to record their spectra simultaneously for calibration of the jet spectrum.

The confocal passive etalon used in the setup had a free spectral range of 0.00997 cm^{-1}. The reference cell was made up of a glass cylinder with a length of 300 mm, a diameter of 45 mm and two calcium fluoride (CaF_2) windows at the ends. The reference cell was filled with a gas that had precisely-known transitions in the frequency region of interest. N_2O gas was used as the reference gas in the study of the $N_2O - (C_2H_2)_2$ clusters.

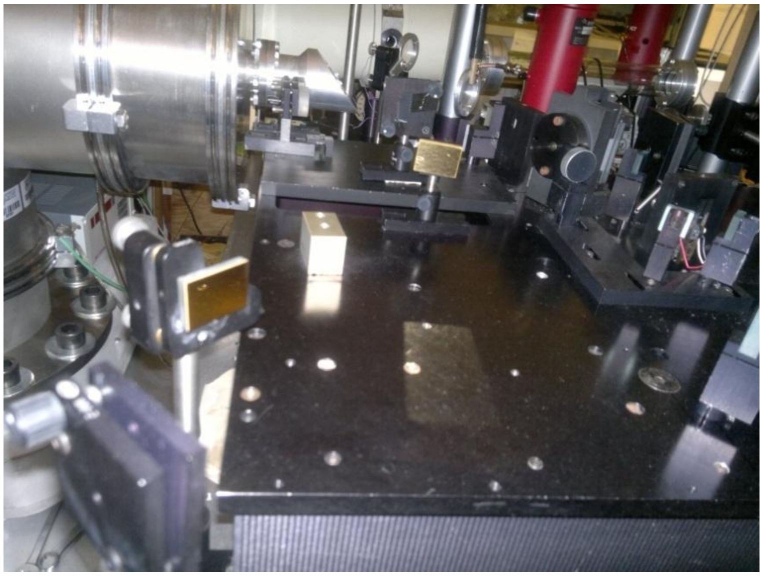

Figure 4.6: Two gold-coated flat mirrors that direct the QCL radiation into the optical setup

There was one mercury cadmium telluride (HgCdTe) and two indium antimonide (InSb) Infrared Associate photovoltaic detectors, which work at liquid nitrogen temperature. Therefore, they were used to convert the optical signals after the jet, etalon and reference gas into electrical signals.

To enhance the sensitivity of the spectrometer an astigmatic multi-pass optical cell was mounted inside the jet chamber based on a new Focus Model 5612 Astigmatic Cell, which is shown in Figure 4.7.

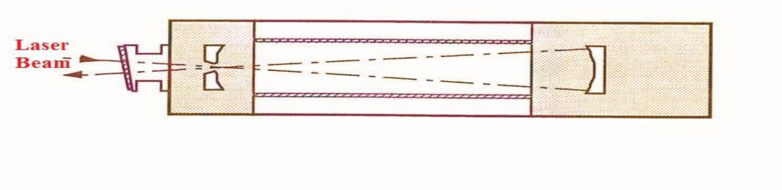

Figure 4.7: Cross section of the body of multi-pass cell adapted from AERODYNE RESEARCH, INC.s' manual

Using the multi-pass cell the number of laser passes can be increased, ranging from 86 to 366 depending on the incident beam angle. The system used in observation of the planar isomer of N_2O-$(C_2H_2)_2$, was optimized for over 100 passes. Figure 4.8 shows the theoretical spot pattern for 182 passes.

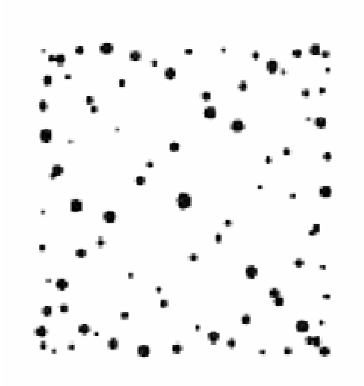

Figure 4.8: Theoretical spot pattern for N = 182 adapted from AERODYNE RESEARCH, INC.s' manual

The number of passes can be increased by changing the mirrors separation and position of the beam_angle for the specific number of passes which is shown in Figure 4.9.

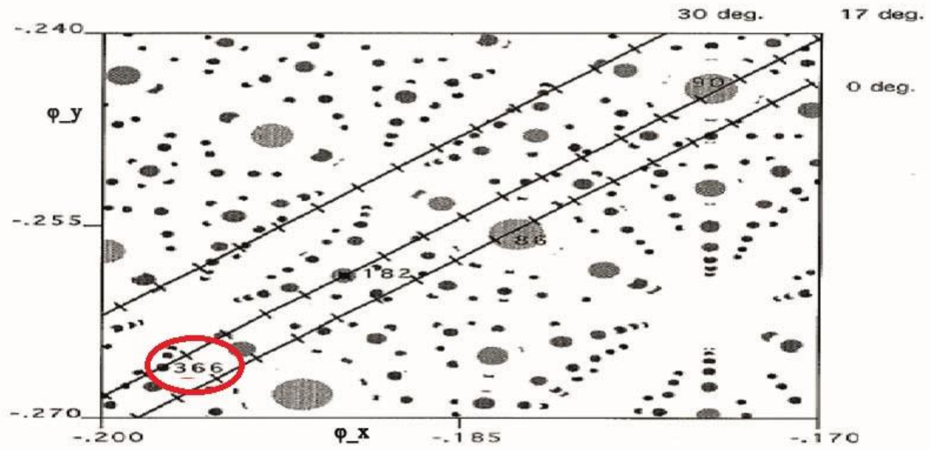

Figure 4.9: Pattern map of locations of commonly used near confocal passes in an astigmatic cell [62].

The equations for the position of the spots are [62]:

$$x_i = X_0 \sin(i\Phi_x) \qquad\qquad y_i = Y_0 \sin(i\Phi_y)$$
$$\Phi_{x,y} = sin^{-1}\left(\frac{D}{R_{x,y}} - 1\right) \tag{4.5}$$

where x_i and y_i are the coordinates of the ith beam spot, X_0 and Y_0 represents the size of the overall spot pattern, D is the mirror separation and $R_{x,y}$ are the mirror radii of the curvature. One can find $\Phi_{x,y}$ from Figure 4.9 and use it in Equation 4.5 to find D.

4.4 Data Acquisition

The data acquisition system was comprised of three parts: data acquisition hardware, data acquisition software and control components (See Figure 4.1).

4.4.1 Data Acquisition Electronics

Electronic instruments, such as a QCL controller, a function generator, a jet valve controller, and counter-timer card were the control components of the setup: A QCL controller (model 1001 TLC Daylight Solution) was used to tune the QCL wavelength by rotating the internal grating rotation, current and/or temperature (Figure 4.10).

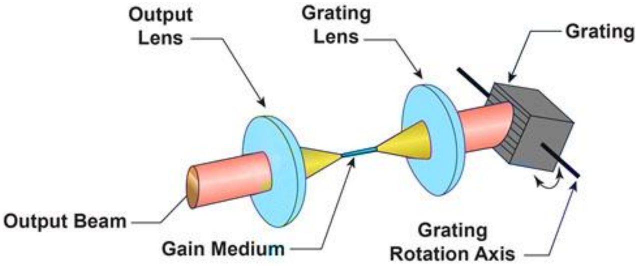

Figure 4.10: Cavity of QCL: The grating and the gain medium where the cascade process happens are shown in the figure [53].

The laser was rapidly scanned across a specific wavenumber region (~0.75 cm^{-1}) at a rate of 100 Hz using a function generator (Wavetek 395, shown in Figure 4.1). The function generator provided a sine-wave to sweep the laser frequency and a trigger signal to synchronize the data acquisition and valve controllers.

As it was mentioned before, the Iota One valve controller controls the opening and closing times of the pulse valves and repetition rate of it in a range of minutes, seconds, milliseconds and microseconds. In our setup, the opening time for each valve was 2.5 ms and the repetition rate was 0.5-1 Hz.

A CTRO5 counter-timer card controlled the timing of the DAQ card with that of the pulsed valves. A LabVIEW-based program developed in the Laser Spectroscopy Laboratory at the University of Calgary controlled both DAQ card and CTRO5.

In the setup, a 2-channel gated boxcar averager was employed to avoid the long-term wavelength drift of the QCL. The signals (a and b) from both sides (maximum slope) of a relatively strong reference line were subtracted to generate an error signal which was applied to the lock circuit. The circuit consisted of two op-amps. The first op-amp was used to invert the error signal sent by the boxcar averager. The second op-amp was used to add the sine-wave created by function generator and the inverted error signal together; the resulting signal was applied to the piezo controller. If the QCL drifted in frequency, the output signal (*b*-*a*) would be non-zero. This feedback shifted the spectral region of the QCL so that the voltage difference between the two gates became zero again.

The electric signals from the detectors needed to be digitized in order to be used in the computer. To digitize the electric signals, a 12-bit DAQ card was used. The timing of the DAQ card was controlled by the CTRO5 counter timer. The DAQ card was triggered by the CTRO5 when the second cycle of the trigger signal was generated by the function generator. The DAQ card digitized data at the rate of 10 MHz over the 1.6 ms time intervals. Moreover, the CTRO5 triggered the valve controllers after 0.5 ms. The user determined the opening time of the valves to be 7.5 ms after receiving the first cycle of the trigger signal. But because of the T ms delay in the mechanical response of the valves to the trigger signals, the valves were completely opened immediately after 7.5+T ms (Figure 4.11). The data acquisition process began after 9.2 ms to avoid recording the data during the opening of the valves.

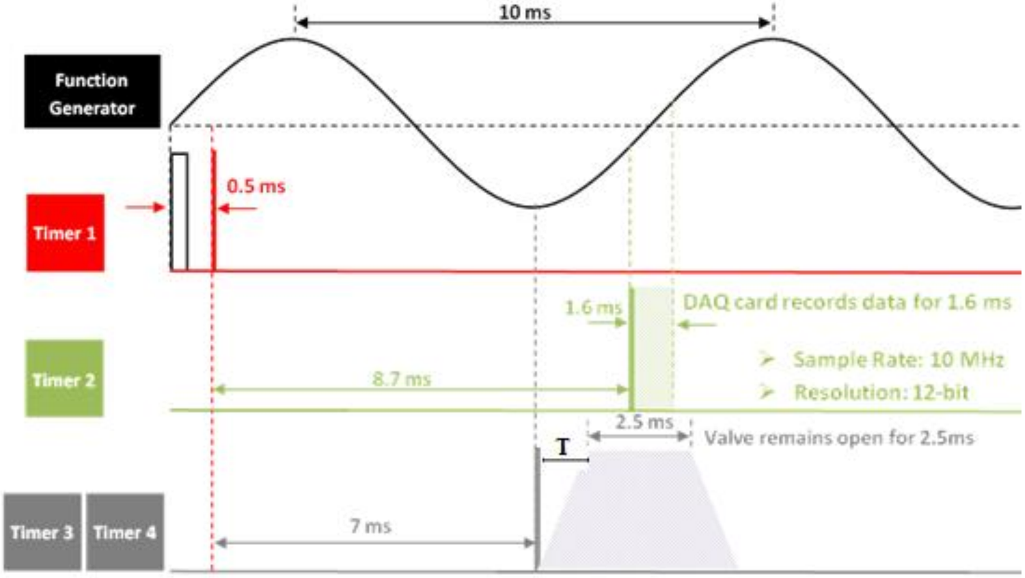

Figure 4.11: Diagram of time sequence of data acquisition

A user was able to change the timing of the spectrometer with the LabVIEW-based program. While the first scan was being taken, the jet valves were closed and only the background absorption is recorded. When the valves were fully opened the jet signal was recorded. The program then subtracted the first scan from the second scan to provide the background-removed jet spectrum. The whole sequence illustrated in Figure 4.11 was repeated at a rate of 1-0.5 Hz. Between the two successive scans the diffusion pump, pumped out the residual gas in the chamber.

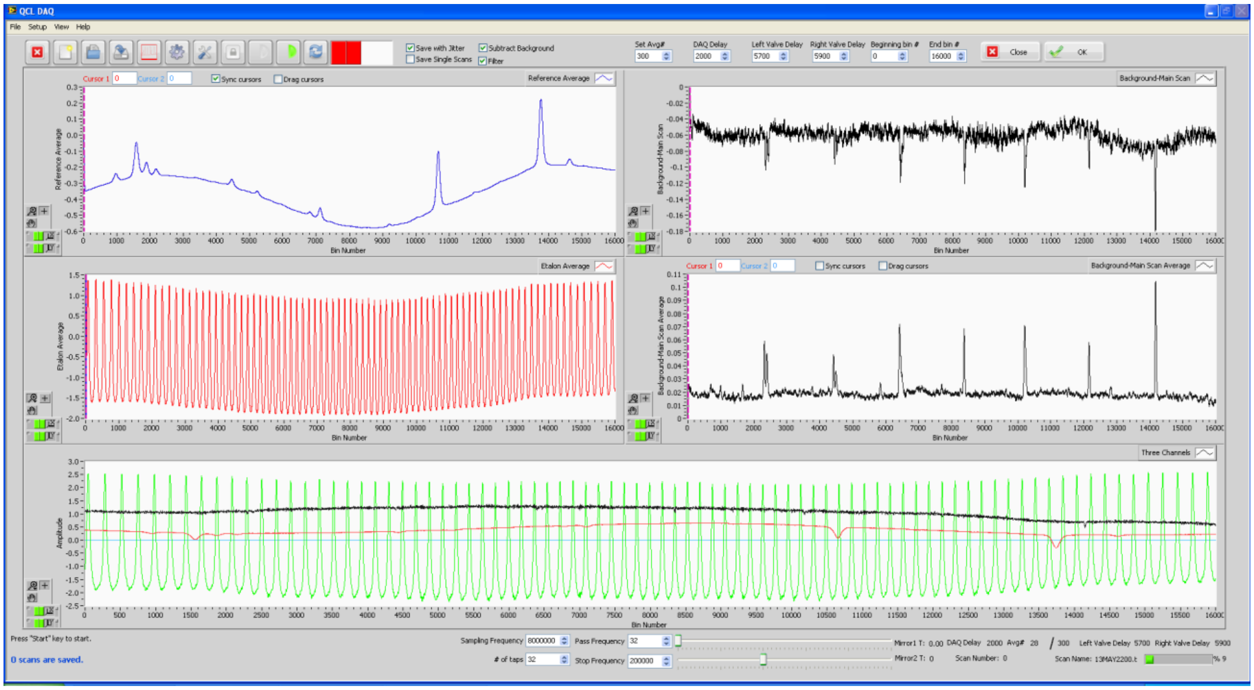

☑ Save with Jitter
☐ Save Single Scans
☑ Subtract Background
☑ Filter
Set Avg# 300
DAQ Delay 2000
Left Valve Delay 5700
Right Valve Delay 5900
Beginning bin # 0
End bin # 16000

Press "Start" key to start.
0 scans are saved.
Sampling Frequency 8000000
# of taps 32
Pass Frequency 32
Stop Frequency 200000
Mirror1 T: 0.00 DAQ Delay 2000 Avg# 28 / 300 Left Valve Delay 5700 Right Valve Delay 5900
Mirror2 T: 0 Scan Number: 0 Scan Name: 13MAY2200.t % 9

Figure 4.12: Snapshot of the main panel of the LabVIEW-based program

In Figure 4.12, the main panel of the LabVIEW-based program is shown. The two windows on the top left are the average reference and the average etalon. The two windows on the top right are the background subtracted jet scan and its average (400 scans were averaged for each isotoplogues spectra in this experiment). The window on the bottom is the jet, reference and etalon signals together in a single scan. The window on the top shows the time parameters for the DAQ card controller.

4.5 Post-data Acquisition

The LabVIEW program stored the intensities in terms of bin numbers; however, for analyzing the data, they should be converted to frequencies or wavenumbers. This was done by a calibration program which uses GRAMS^{TM} as a plat form. The calibration software took the known transition frequencies of the recorded reference gas as an input. The software then interpolated the recorded, jet spectrum using these transition frequencies and the etalon peaks. In Figure 4.13, the first spectrum from the top is the background removed jet signal, the middle one is the reference gas spectrum, and the bottom trace is the etalon spectrum.

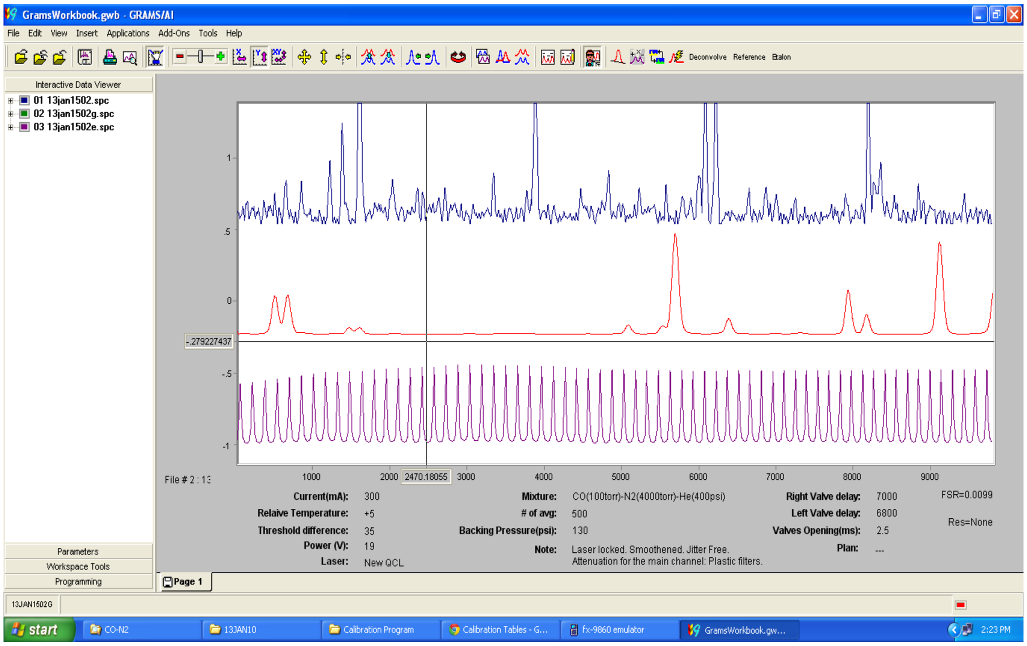

Current(mA): 300
Relaive Temperature: +5
Threshold difference: 35
Power (V): 19
Laser: New QCL
Mixture: CO(100torr)-N2(4000torr)-He(400psi)
# of avg: 500
Backing Pressure(psi): 130
Note: Laser locked. Smoothened. Jitter Free. Attenuation for the main channel: Plastic filters.
Right Valve delay: 7000
Left Valve delay: 6800
Valves Opening(ms): 2.5
Plan: ---
FSR=0.0099
Res=None

Figure 4.13: Snapshot of the GRAMS software

After calibration, the data were ready for final analysis by PGOPHER software, which is a program for simulating the rotational vibrational spectra [63]. Figure 4.14 shows the main window of the PGOPHER program. The panel on the right side of the main window contains information about the rotational constant for ground and excited states, centrifugal distortion parameters, vibration-rotation parameters, symmetry, etc.

The simulation for N_2O – $(C_2H_2)_2$ was done by pre-calculating the rotational constants (A, B, C) of the cluster based on an assumed structure using the PMIFST program [64], assuming the symmetry species of the vibrational states and the spin statistical weights of the rotational states. The rotational constants were calculated using the cluster calculation program which is explained in the chapter 5.

The calibrated spectrum needed to be fitted to the model Hamiltonian. In the fitting process, the rotational constants and distortion parameters could be varied (Figure 4.14). To show the accuracy of the fit, PGOPHER calculated the root mean square of the observed frequencies and the corresponding calculated frequencies (Equation 4.6):

$$\Delta\vartheta_{rms} = \sqrt{\frac{1}{N}\sum_{i=1}^{N}(\vartheta_i^{obs.} - \vartheta_i^{cal.})^2} \tag{4.6}$$

Fitting the observed transitions to simulated spectrum is essentially solving an inverse eigenvalue problem (Section 3.1).

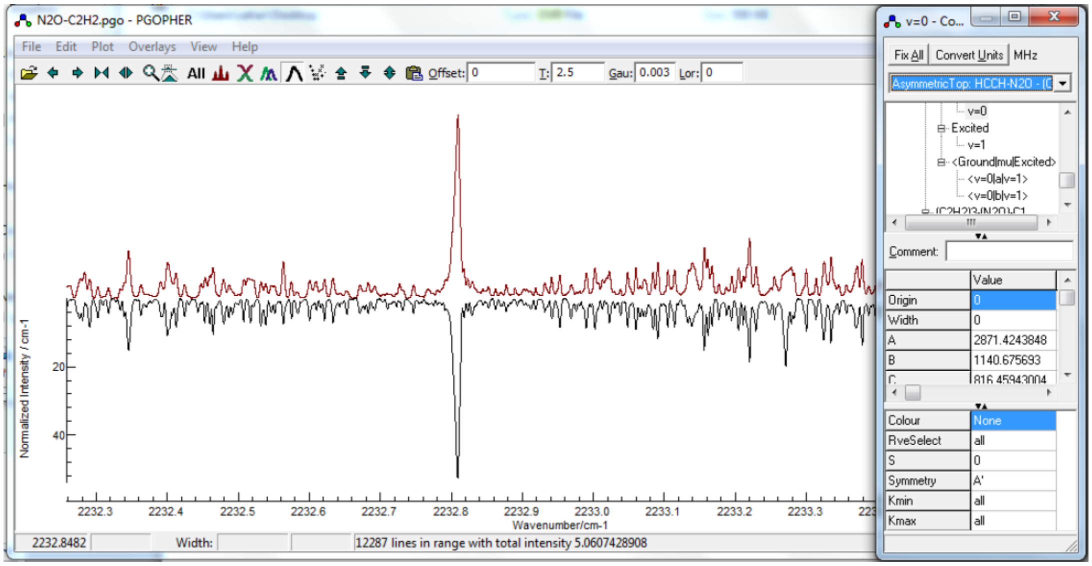

Offset: 0 T: 2.5 Gau: 0.003 Lor: 0

AsymmetricTop: HCCH-N20 - (C

Comment:

	Value
Origin	0
Width	0
A	2871.4243848
B	1140.675693
C	816.45943004

Colour	None
RveSelect	all
S	0
Symmetry	A'
Kmin	all
Kmax	all

2232.8482 Width: 12287 lines in range with total intensity 5.0607428908

Figure 4.14: Snapshot of the PGOPHER program. The window on the right side contains information, such as rotational constants, centrifugal distortion parameters, etc. for ground state and excited states. Red and black spectra are the observed and simulated spectra, respectively.

Chapter 5: Observation of a Planar Isomer of the $N_2O – (C_2H_2)_2$ Trimer

The experimental results of the study on $N_2O – (C_2H_2)_2$ trimer are discussed. The semi-empirical calculation that was done on the observed planar isomer of $N_2O – (C_2H_2)_2$ to calculate the theoretical structure is explained. The calculated results are then compared with the experimental results.

5.1 Formation and Observation of $N_2O – (C_2H_2)_2$ Cluster

The weakly bound $N_2O – (C_2H_2)_2$ clusters were formed using a gas mixture of 10 Torr of N_2O, 90 Torr of C_2H_2 and 400 psi of helium (He) in the pulsed supersonic jet. Because the band origin of this trimer was not previously known, the experiment was started by recording search scans around the N_2O fundamental band origin (~2224 cm^{-1}) with a mixture consisting of 33 Torr of N_2O, 66 Torr of C_2H_2 and 400 psi of He. Two sharp features were observed around 2240 cm^{-1} and 2224 cm^{-1} with the latter being about 2 times stronger than the former. Attempts to simulate the band around 2240 cm^{-1} and 2224 cm^{-1} with the calculated rotational constants were unsuccessful. However, optimizing the mixture in favour of C_2H_2 and performing search scans around (N_2O) ν_1 fundamental band origin resulted in appearance of a sharp feature at 2232.8 cm^{-1} which turned out to be the Q-branch of the planar $N_2O – (C_2H_2)_2$ band. Eventually this band was recorded with a mixture of 10 Torr of N_2O, 90 Torr of C_2H_2 and backing pressure of 120 psi.

This vibrational band has been recorded and observed by exciting the ν_1 fundamental band of N_2O using a QCL. It is blue shifted by 9 cm^{-1} with respect to the N_2O fundamental band origin and was determined to be an a/b-type hybrid band.

5.1.2 Structure Determination

One can write the moment of inertia tensor of a molecule in terms of the position of atoms on the principal axes coordinate system. If m_i is considered as the mass of the i_{th} atom, and (a_i, b_i, c_i) is the coordinates of that atom. The relationships for diagonal elements are given as:

$$\begin{aligned} I_a &= \sum m_i(b_i^2 + c_i^2) \\ I_b &= \sum m_i(a_i^2 + c_i^2) \qquad (5.1) \\ I_c &= \sum m_i(a_i^2 + b_i^2) \end{aligned}$$

Since two bond lengths and four angles are needed to determine the structure of planar isomer of $N_2O - (C_2H_2)_2$, three rotational constant parameters are inadequate to determine its structure. As a result, the spectra of two isotopically substituted clusters of $^{15}N_2O - (C_2H_2)_2$ and $N_2O - (C_2D_2)_2$ were also recorded.

These additional spectra provided two more sets of rotational constants. For each isotopologue, semi-empirical rotational constants were also calculated to obtain good starting points for frequency analyses of the bands. Observed and simulated spectra for the three isotopologues are shown in Figures (5.1)-(5.3). The corresponding experimental rotational constants are listed in Tables (5.1)-(5.3). Here the assumption is made that the geometry of the cluster is invariant under isotopic substitution.

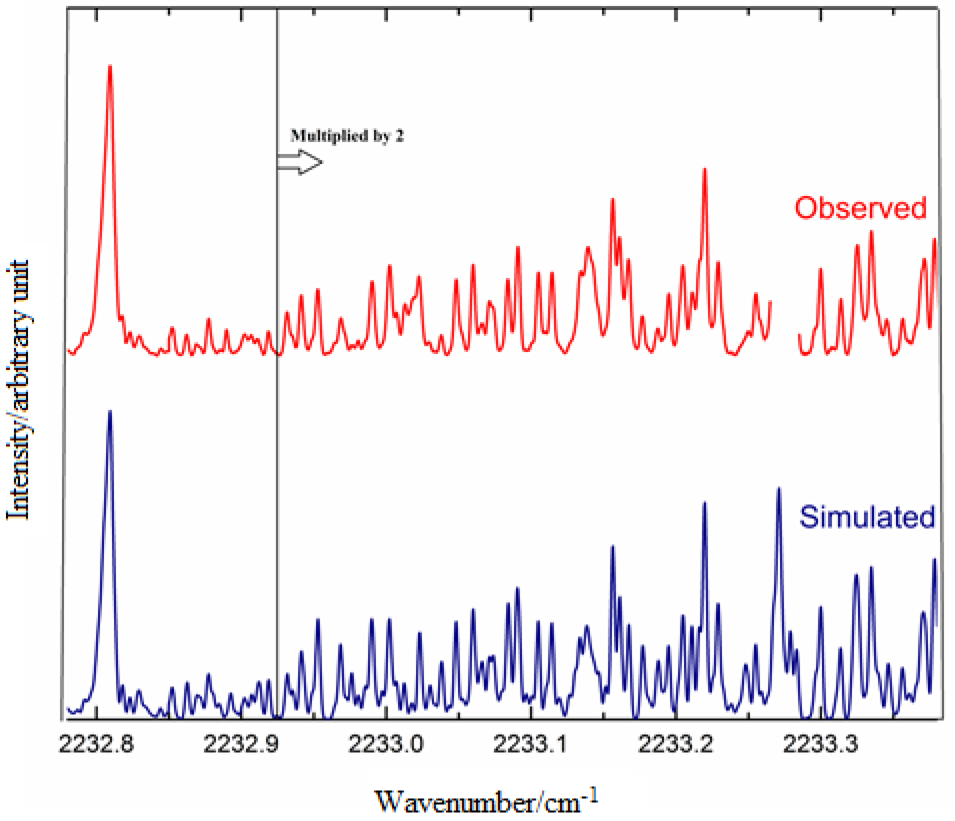

Figure 5.1: Q- and R-branch of the observed and simulated spectra of the planar $N_2O - (C_2H_2)_2$. The root mean square error of the fit is 0.0003 cm^{-1}. The intensities were multiplied by a factor of 2 after 2232.925 cm^{-1}. The simulated spectrum used a rotational temperature of 2.5 K. The gap is related to N_2O monomer absorption around 2232.25 cm^{-1}.

Table 5.1: Experimental rotational constants of planar $N_2O - (C_2H_2)_2$ in ground and excited states (The rotational constants with double prime superscript are the ground state and those with prime are the excited state.)

ν_o/cm^{-1}	2232.812443(62)
A''/MHz	2871.4(11)
B''/MHz	1140.67(20)
C''/MHz	816.46(14)
A'/MHz	2866.04(93)
B'/MHz	1138.58(17)
C'/MHz	814.92(13)
$\Delta\nu_o$/cm^{-1}	9.1
Inertial defect/Amu. Å^2	0.11

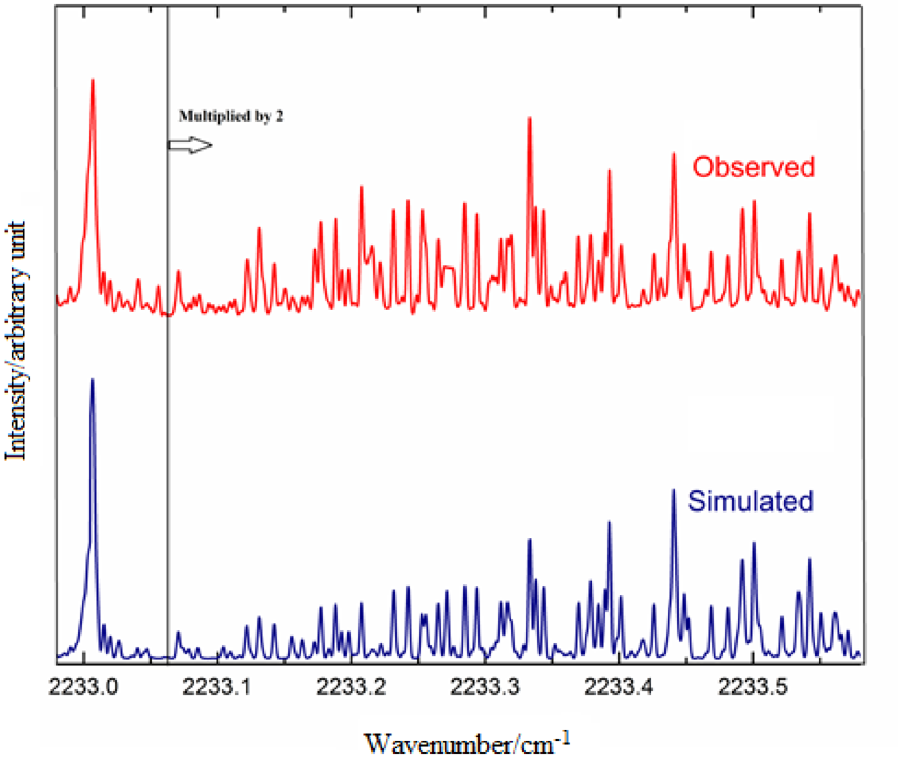

Figure 5.2: Q- and R-branch of the observed and simulated spectra of the planar $N_2O - (C_2D_2)_2$. The root mean square error of the fit is 0.0002 cm^{-1}. The intensities were multiplied by a factor of 2 after 2233.051 cm^{-1}. The simulated spectrum used a rotational temperature of 2.5 K.

Table 5.2: Rotational constants of planar $N_2O - (C_2D_2)_2$ in ground and excited states (The rotational constants with double prime superscript are the ground state and those with prime are the excited state.)

$\boldsymbol{v}_o$/cm^{-1}	2233.009801(49)
A''/MHz	2690.58(87)
B''/MHz	1072.70(13)
C''/MHz	767.584(95)
A'/MHz	2684.84(79)
B'/MHz	1070.78(13)
C'/MHz	766.253(94)
$\Delta\boldsymbol{v}_o$/cm^{-1}	9.2
Inertial defect/Amu. Å^2	0.55

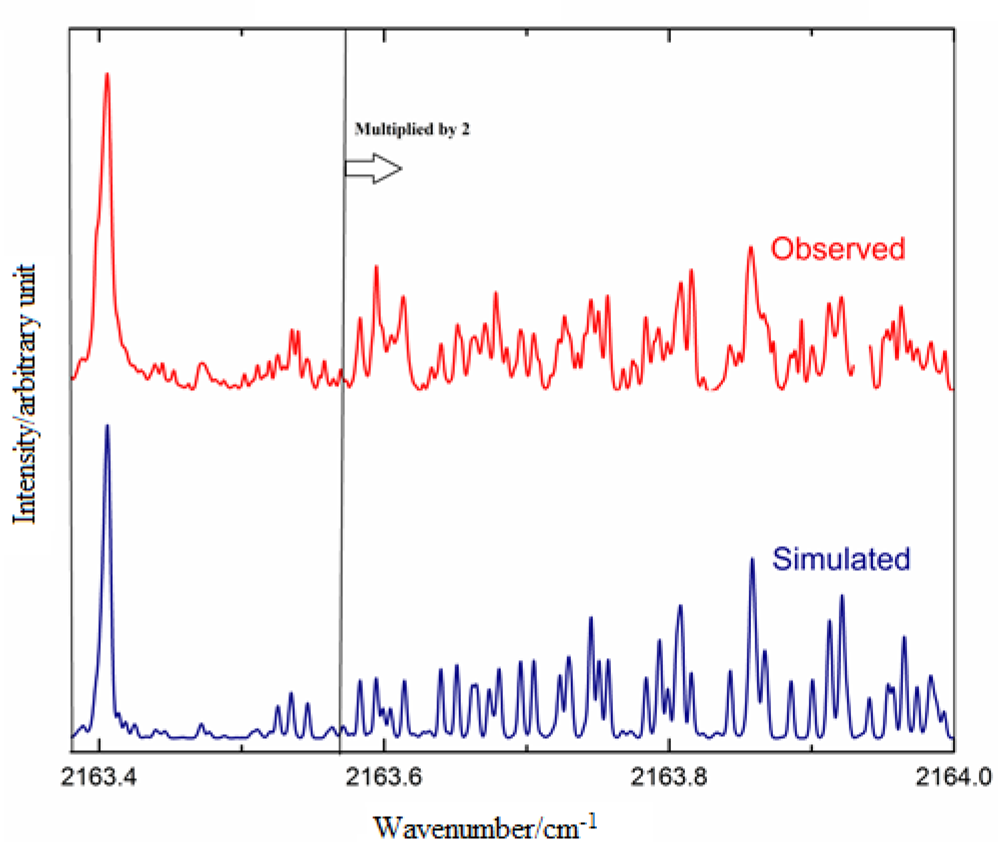

Figure 5.3: Q- and R-branch of the observed and simulated spectra of the planar $^{15}N_2O-(C_2H_2)_2$. The root mean square error of the fit is 0.0003 cm^{-1}. The intensities were multiplied by a factor of 2 after 2163.53 cm^{-1}. The simulated spectrum used a rotational temperature of 2.5 K. The gap is related to N_2O-He absorption around 2263.9 cm^{-1}.

Table 5.3: Rotational constants of planar $^{15}N_2O-(C_2H_2)_2$ in ground and excited states (The rotational constants with double prime superscript are the ground state and with prime are the excited state.)

$\boldsymbol{\nu}_o$/cm^{-1}	2163.408419(63)
A''/MHz	2841.6(59)
B''/MHz	1114.83(18)
C''/MHz	801.89(21)
A'/MHz	2838.2(59)
B'/MHz	1112.75(19)
C'/MHz	800.62(22)
$\Delta\boldsymbol{\nu}_o$/cm^{-1}	8.3
Inertial defect/Amu. Å ^{2}	0.99

5.1.3 Semi-empirical Calculation

A good approximate structure simplifies analysis of the spectrum. Therefore, predicting the structure by semi-empirical calculations serves as a good starting point. The calculated structures used in this experiment were based on the lowest energy minimum structure, which was obtained from semi-empirical cluster calculations developed by our group. Approximate structures for the first few lowest energy minima were found based on Muenter's distributed multipole potentials (for N_2O and C_2H_2) and the Powell minimization method [65].

The program started by defining the parameters needed for Muenter's distributed multipole potentials for OCS, C_2H_2, N_2O, or CO_2 [66] whichever is present in in our spectra using the gas mixture.. In this model, the total interaction energy between molecule a and b ($U(ab)$) is assumed to be the sum of repulsion, dispersion and electrostatic contributions [23]:

$$U(ab) = U^{ab}_{rep.} + U^{ab}_{disp.} + U^{ab}_{elec.} \tag{5.2}$$

where the first two terms are represented by the Lennard-Jones potential:

$$U^{ab}_{rep.} + U^{ab}_{disp.} = \sum_{ij} \left(\frac{C^{ab}_{12}(ij)}{R^{12}} - \frac{C^{ab}_{6}(ij)}{R^{6}} \right) \tag{5.3}$$

In the above equation, $C^{ab}_{12}(ij)$ and $C^{ab}_{6}(ij)$ are Lennard-Jones parameters for the i_{th} atom of molecule a interacting with the j_{th} atom of molecule b. The electrostatic potential can be written as a function of point charges (q), dipole moments (μ) and quadrupole moments (θ), which are located at atoms or mid-bond positions [23]:

$$\begin{aligned} U^{ab}_{elec.} = \sum_{kl} \big(& q^a_k q^b_l F(q_k q_l) + q^a_k \mu^b_l F(q_k \mu_l) + q^a_k \theta^b_l F(q_k \theta_l) \\ & + \mu^a_k \mu^b_l F(\mu_k \mu_l) + \mu^a_k \theta^b_l F(\mu_k \theta_l) + \theta^a_k \theta^b_l F(\theta_k \theta_l) \\ & + \mu^a_k q^b_l F(\mu_k q_l) + \theta^a_k q^b_l F(\theta_k q_l) + \theta^a_k \mu^b_l F(\theta_k \mu_l) \big) \end{aligned} \tag{5.4}$$

In Equation 5.4, k and l are used instead of i and j to indicate that the multipole moments do not need to be located only at the atoms. Furthermore, $F(m_k m_l)$ shows that m_k and m_l geometrically depend on the energy of the interaction between m_k and m_l multipole moments [23].

The program generates N-1 random centres of mass for molecules 2, 3, 4, ... N and then uses cylindrical coordinates centred on molecule number 1. The cylindrical coordinates simplify the randomization. The position of molecule number 2 is determined by its centre of mass distance and angle to molecule number 1. But the position and orientation of molecule number 1 is arbitrary, and one coordinate for molecule number 2 is arbitrary because of the cylindrical symmetry around molecule number 1. Alternately, we can say that the overall position of the cluster itself is arbitrary, and the overall orientation of the cluster itself is arbitrary (this requires 3 angles). These positions and orientations components are converted to Cartesian coordinates of atoms in principal coordinate system of the molecules centered on centre of mass. However, if these random values are close to the previous values, the program goes back and generates a new set of values. The random orientation is determined by running the longitudinal angle from 0 to 2π and latitudinal angle from 0 to π; therefore, it generates two-dimensional variable ($\mathrm{x_i} = (\theta_\mathrm{i}, \varphi_\mathrm{i})$) and uses the Powell method to return with the minimized cluster energies and associated structures [67].

The cluster calculation software was used to determine the rotational constants of the two lowest energy isomer of the $N_2O - (C_2H_2)_2$. The program ran for 5000 iterations to find energy minima on the potential surface of the trimer.

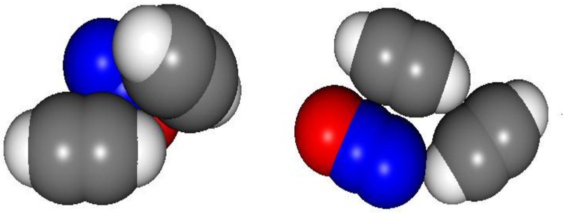

Figure 5.4: Loose-barrel-shaped structure of $N_2O - (C_2H_2)_2$ is shown on the left side of the figure, and the planar isomer is on the right side of the figure. The lowest energy isomer is shown on the right and the second lowest energy isomer is shown on the left.

Table 5.4: Binding energies and rotational constants for the two lowest energy isomers of the $N_2O - (C_2H_2)_2$ trimer as given by the present semi-empirical potential.

	Planar	Nonplanar, Distorted barrel shape
E/cm^{-1}	-1496	-1414
A/MHz	3142	2174
B/MHz	1075	1788
C/MHz	801	1229

Aided by these calculated rotational constants, the observed spectra were simulated and resulting rotational constants obtained are those listed in Tables (5.1)-(5.3).

5.2 Geometrical Properties of Planar N_2O – $(C_2H_2)_2$

As discussed in Chapter 2, the inertial defect is given by:

$$\Delta = I_c - I_a - I_b \tag{5.5}$$

If this value is approximately zero, then the structure would be planar. For an exactly planar structure, Equation 5.6 can be utilized:

$$\frac{1}{C} = \frac{1}{A} + \frac{1}{B} \tag{5.6}$$

In the case of the observed N_2O – $(C_2H_2)_2$, the inertial defect was 0.11 amu.Å^2, which is small enough to conclude that the cluster is planar. The inertial defect may be due to zero-point energy, or the precision in the experimentally determined rotational constants.

The geometrical structure of the cluster is determined by its rotational constants. The structure determination for the related planar dimer of N_2O – C_2H_2 is demonstrated analytically below. Calculating the geometry for N_2O – $(C_2H_2)_2$ is more complicated but the same principles hold true. To determine the structural parameters of the planar N_2O – C_2H_2 dimer, only three parameters are required (Figure 5.5). The first parameter (R) is the distance between the centre of mass of C_2H_2 and N_2O, the second parameter is the angle between (R) and the N_2O monomer axis (θ), and the third is the angle between the C_2H_2 monomer axis and the x axis (α). This goal is achieved by writing the moment of inertia tensor in centre of mass coordinate system, using the parallel axis theorem and diagonalizing it, through the consideration of Equations 5.1, 5.7 and 5.8.

$$I_{\alpha\beta} = -\sum_i m_i x_{\alpha i} x_{\beta i} \tag{5.7}$$

$$\mu = \frac{m_{N2O} m_{C2H2}}{m_{N2O} + m_{C2H2}} \tag{5.8}$$

The moment of inertia tensor in terms of the polar cylindrical coordinate system is written as:

$$I_{xx} = \mu R^2 (sin\theta)^2 + I_{\mathrm{C_2H_2}} (sin\alpha)^2$$

$$I_{xy} = I_{yx} = -\mu R^2 sin\theta cos\theta - I_{\mathrm{C_2H_2}} sin\alpha cos\alpha + \beta sin\theta$$

$$I_{yy} = \mu R^2 (cos\theta)^2 + I_{\mathrm{C_2H_2}} (cos\alpha)^2 + I_{\mathrm{N_2O}} - 2\beta cos\theta \qquad (5.9)$$

$$I_{zz} = \mu R^2 + I_{\mathrm{C_2H_2}} + I_{\mathrm{N_2O}} - 2\beta cos\theta$$

$$I_{xz} = I_{zx} = I_{yz} = I_{zy} = 0$$

In determining cluster structures, the following two assumptions are made:

1. Structures of monomers do not change upon complex formation.
2. Isotopic substitution does not change the complex structure.

In Equation 5.10, $I_{\mathrm{C_2H_2}}$ and $I_{\mathrm{N_2O}}$ are the moments of inertia of C_2H_2 and N_2O, respectively, and β is defined as:

$$\beta = \frac{\mu R}{m_{\mathrm{N_2O}}} (m_N (R_{\mathrm{NN}} + 2R_{\mathrm{N}C}) - m_{\mathrm{O}} (R_{\mathrm{o}c})) \qquad (5.10)$$

where R_{NN}, $R_{\mathrm{N}C}$,and $R_{\mathrm{O}C}$ show the bond lengths of the terminal N – middle N, middle N – N_2O's centre of mass, and O – N_2O's centre of mass , respectively, and they are assumed to be constant.

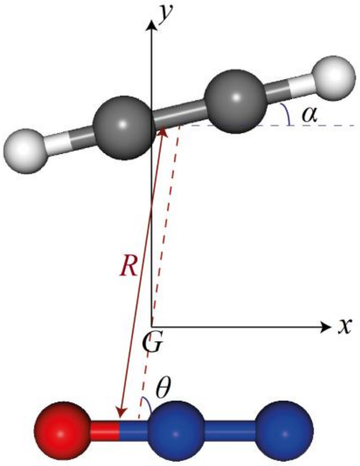

Figure 5.5: Structural parameters for the $N_2O - C_2H_2$ dimer

One can find the eigenvalues of the moment of inertia matrix and substitute them with the principal moments of inertia ($I_c \geq I_b \geq I_a$) to find α, θ and R.

The method for finding the structure of N_2O – C_2H_2 has been explained; however, in the case of N_2O – $(C_2H_2)_2$, the theoretical calculation is even more complex, due to the need for calculations for three monomers and for the determination of values of 6 different parameters in order to find the geometrical structure of the cluster. The results of the cluster calculation program are transformed into structural parameters (bond lengths and angles) with PMIFST software [64], which are presented in Table 5.5.

Table 5.5: Theoretical structural parameters (Here, R and θ stand for bond-length and angle, respectively. The atom numbering are shown in Figure 5.6.)

Structural Parameters:	Theoretical Values:
$R(10,1)$	5.04 Å
$R(5,1)$	3.29 Å
$\theta(5,1,2)$	85.3°
$\theta(6,5,1)$	100.3°
$\theta(10,1,2)$	27.4°
$\theta(11,10,1)$	33.1°

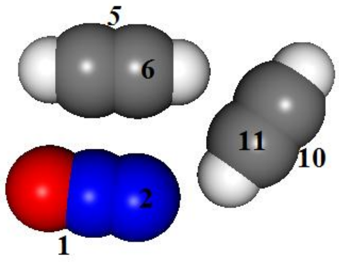

Figure 5.6: Theoretical structure of the planar N_2O-$(C_2H_2)_2$ trimer. Number 1 shows the centre of mass of N_2O, numbers 5 and 10 are the centre of masses of the two acetylenes. Numbers 2, 6 and 11 are nitrogen, carbon and carbon atoms, respectively.

We used the calculated geometry and experimental rotational constants to fit the structure to the experiment using STRFIT software [68]. Starting with the calculated structures, we experimented with different alterations and arrived at a semi-experimental structure that was in good agreement with the spectroscopic data. This software uses the reverse calculation of the PMIFST program. The results are shown in Table 5.6. The numbers for the bond length and angles in Table 5.6 are related to the labels in Figure 5.7.

Table 5.6: Experimental structural results (Here, *R* and θ stand for bond-length and angle, respectively. The atom numbering are shown in Figure 5.7.)

Structural Parameters:	Experimental Values:
R(10,1)	4.79(1) Å
R(5,1)	3.97(3) Å
θ *(5,1,2)*	74˚(5)˚
θ *(6,5,1)*	100.3˚
θ *(10,1,2)*	28˚(5˚)
θ *(11,10,1)*	33.1˚

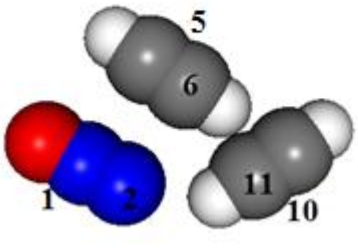

Figure 5.7: Experimental structure of the planar N_2O – $(C_2H_2)_2$ trimer. Number 1 shows the centre of mass of N_2O, and numbers 5 and 10 are the centre of masses of the two acetylenes. Numbers 2, 6 and 11 are the nitrogen, carbon and carbon atoms, respectively.

As can be seen in Table 5.6, two of the angles (θ *(6,5,1)* and θ *(11,10,1)*) in this structure could not be determined. As a result, the theoretical angles were chosen to use instead of those two angles for demonstration of the structure. These angles were fixed at their values from the cluster calculation during the structural fit. The inability to determine these angles may be related to the difficulty in determining the structure of the very similar cluster of OCS – $(C_2H_2)_2$ [18, 35]. Probably, the reason is related to aptitude of inter-conversion tunneling motion in the C_2H_2 pair inside the trimer. As it was discussed in section 3.8, the inter-conversion tunneling motion causes splittings in energy levels. However, we did not observe any splittings in the energy levels, maybe due to insufficient resolution of the experiment (75 MHz), the large amplitude motion of the acetylene units is still possible(See Chapter 3).

In the Table 5.7, the rotational constants, vibrational shift and inertial defect of N_2O – $(C_2H_2)_2$ and OCS – $(C_2H_2)_2$ are compared [18]. The small inertial defects in both complexes are evidence for planarity of the two complexes. Also, semi-empirical and experimental structures of the two planar isomers of the OCS – $(C_2H_2)_2$ and N_2O – $(C_2H_2)_2$ are compared in Table 5.8. As it can be seen, the structural parameters for the two lowest energy isomers are fairly close to each other theoretically and experimentally which support the assumption of close structures for the two isomers (See Chapter 1 and 2). Also, the semi-empirical calculations show that the structure for the second lowest energy isomer of N_2O – $(C_2H_2)_2$ is very similar to the structure which was determined experimentally for the second lowest energy isomer of OCS – $(C_2H_2)_2$ (See Section 2.5) [35].

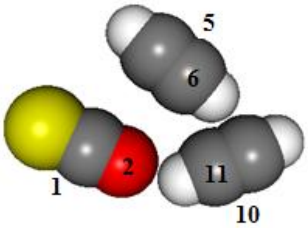

Figure 5.8: Experimental structure of the planar OCS – $(C_2H_2)_2$ trimer. Number 1 shows the centre of mass of OCS, and numbers 5 and 10 are the centre of masses of the two acetylenes. Numbers 2, 6 and 11 are the oxygen, carbon and carbon atoms, respectively.

Table 5.7: Comparing semi-empirical and experimental rotational constants and vibrational shifts for OCS – $(C_2H_2)_2$ and N_2O – $(C_2H_2)_2$.

	N_2O – $(C_2H_2)_2$	OCS – $(C_2H_2)_2$
$\boldsymbol{v}_\circ$/cm^{-1}	2232.812443(62)	2058.8460 (2)
A''/MHz	2871.4(11)	2720.9 (71)
B''/MHz	1140.67(20)	792.520 (149)
C''/MHz	816.46(14)	612.342 (128)
A'/MHz	2866.04(93)	2713.9 (71)
B'/MHz	1138.58(17)	792.435 (149)
C'/MHz	814.92(13)	611.968 (125)
$\Delta\boldsymbol{v}_\circ$/cm^{-1}	9.1	-3.355
Inertial defect/Amu. Å^2	0.11	1.90*

*Changing A rotational constant for OCS – $(C_2H_2)_2$ in either direction causes a range of 1.41–2.38 of error for inertial defect.

Table 5.8: Comparing semi-empirical and experimental structural results for OCS – $(C_2H_2)_2$ and N_2O – $(C_2H_2)_2$, the numbers have been shown in Figures 5.7 and 5.8. Here, R and θ stand for bond-length and angle, respectively.

Structural Parameters	Semi-empirical		Experimental	
	N_2O – $(C_2H_2)_2$	OCS – $(C_2H_2)_2$	N_2O – $(C_2H_2)_2$	OCS – $(C_2H_2)_2$*
R(10,1)	5.04 Å	5.664 Å	4.79(1) Å	4.149 Å
R(5,1)	3.29 Å	3.06 Å	3.97(3) Å	5.203 Å
θ *(5,1,2)*	85.3°	75.1	74°(5)°	63
θ *(6,5,1)*	100.3°	75	100.3°	77
θ *(10,1,2)*	27.4°	25	28°(5°)	17
θ *(11,10,1)*	33.1°	29.1	33.1°	15.09

*The structural parameter values for OCS – $(C_2H_2)_2$ are determined semi-experimentally.

Chapter 6: Conclusion and Future Studies

This chapter presents the conclusion and brief discussion on the results of studying N_2O – $(C_2H_2)_2$ complex focusing on rotational constants, geometrical structure and etc. Furthermore, the tunneling effect between the equilibrium structures of the C_2H_2 monomers, which probably causes the inability to determine the precise structure of the complex, is discussed. Then, the required modifications of the experimental setup used in this investigation are explained. Finally, determination of precise molecular structure is proposed for future.

6.1 Conclusion and Discussion

The experiment was undertaken to study the interactions between N_2O and C_2H_2 monomers in the molecular cluster of N_2O – $(C_2H_2)_{2.}$ These clusters were formed in a pulsed supersonic slit-jet expansion. High-resolution infrared spectra of the weakly bound N_2O – $(C_2H_2)_2$ trimer complex have been recorded by exciting the nitrous oxide (N_2O) ν_1 fundamental band (~2224 cm^{-1}) using a quantum cascade laser and fitted to a semi-rigid asymmetric rotor Hamiltonian.

The study has shown that the recorded band is an a/b-type hybrid band with the rotational constants of A =2871.4(11) MHz, B = 1140.67(20) MHz, and C = 816.46(14) MHz, satisfying the condition for a planar structure. In addition to the normal istopologue, $^{15}N_2O$ – $(C_2H_2)_2$ and N_2O – $(C_2D_2)_2$ have been also observed to facilitate the determination of the structure. The precise geometrical configuration of a planar isomer of the N_2O – $(C_2H_2)_2$ could not be made. This is thought to be due to the tunneling motion between C_2H_2 monomers.

The tunneling motion and splitting of energy levels are explained in Sections 3.8 and 3.8.1. The energy level splitting due to the tunneling motion was not observed in the experiment; Perhaps, because it was out of the resolution of our experiment.

6.2 Further Enhancement

In the recorded spectra of the planar isomer of the $N_2O – (C_2H_2)_2$, some of the lines were somewhat broader with lower resolution compared to those of the simulation. Improved resolution could be obtained by minimizing the effect of jittering of the laser. This jittering may cause line broadening. To avoid this issue, a jitter suppression program has been developed by our group. This program measures the shift of the etalon peaks for each single scan with respect to a reference scan due to the jittering of the laser and adds it to the jet signal, so the result would be a jitter-free spectrum. All the reported data was recorded using a QCL. However, the use of an optical parametric oscillator has the advantages that it would allow the extension of the cluster studies to the important C – H, and O – H fundamental regions (2.5-4 μm), where complexes such as $N_2O – C_2H_2$ can be studied at much higher resolution (1 MHz) if a skimmer is used. The higher resolution will be particularly significant as the cluster size grows, because the underlying rotational structure becomes more difficult to fully resolve due to a higher density of states. The higher resolution helps resolving blended lines in spectra recorded in this study which would result in more precise rotational parameters. Therefore, determining the accurate geometrical structure of the trimer could be made possible.

As it is discussed in chapter 4, the number of passes in the astigmatic multi-pass absorption cell can be increased ranging from 86 to 366. Increasing the number of passes increases the signal to noise ratio of the absorption signal. Some studies related to increasing the number of passes to 366 have been done, and it is possible to increase the number of passes in the near future. The mirror system is more stable and less prone to optical interference in the configuration that allows 366 passes.

To achieve a more uniform distribution of the molecular beam along the axis of the slit and to enhance the formation of clusters, especially those containing three or more monomers, a multi-channel block nozzle is used. The current setup utilizes two block nozzles. It may be possible to increase the number of blocks to three in the near future. Using a block nozzle causes an increase in the effective absorption path which enhances the signal to noise ratio. Also, a longer block nozzle causes narrower Doppler line widths [69] which improve the resolution of the spectrum. Furthermore, cooling down the nozzles would help in the formation of the larger clusters.

6.3 Future Studies

To determine the structure of a planar isomer of the $N_2O – (C_2H_2)_2$, more isotopologues such as $^{15}N_2O – (C_2D_2)_2$ and $N_2{}^{18}O – (C_2D_2)_2$ should be considered. Also, this experiment could be done in the microwave region to determine the rotational constants of the complex more precisely or observe splittings of the energy levels as a result of the inter-conversion tunneling motion of the acetylene units.

Moreover, in the higher side of the R branch of the cluster of $N_2O – (C_2H_2)_2$, there are some unknown features which are probably because of the larger clusters. Hence, recording spectra at higher wave-numbers should be continued, in order to find and analyze the larger clusters formed between N_2O and C_2H_2.

References

1. **D. D. Ebbing, S. D. Gammon**, General Chemistry: Media Enhanced Edition, Cengage Learning, 1(2007), p.437

2. **L. Pauling,** General Chemistry, Dover Publications, 1(1970), p.393

3. **R. Clausius,** Annalen der Physik, 79(1850), p.368

4. **T. Andrews,** Philopsophical Transcations of the Royal Society of London, 159 (1869, p. 575

5. **I. Muller, W. H. Muller,** Fundamentals of Thermodynamics and Applications: With with Historical Annotations and Many Citations from Avogadro to Zermelo, Springer, 1(2009), p.79

6. **V. Vedral, J. A. Dunningham,** Introductory Quantum Physics and Relativity, Imperial College press, 1(2010), p.99

7. **W. Demtroder,** Molecular Physics, Wiley-VCH, 1(2008), p.343

8. **W. Herschel,** Philosophical Transactions of Royal Soceity of London, 90(1800), p. 255

9. **M. D. Kelleher, R. K. Shah, K. R. Sreenivasan, Y. Joshi**, Experimental Heat Transfer, Fluid Mechanics and Thermodynamics, Elsevier, 1(1993), p.187

10. **W. Abney, E. R. Festing,** Philosophical Transactions of the Royal Society of London, 172(1881), p.887

11. **W. W. Coblentz,** Carnegie institution of Washington, 35(1905), p.101

12. **I. Rehman, Z. Movasaghi, S. Rehman**, Vibrational Spectroscopy for Tissue Analysis, CRC Press, 1(2012), p.8

13. **T. Visser**, Encyclopedia of Analytical Chemistry, 1(2006)

14. **K. Nakamoto**, Infrared and Raman Spectra of Inorganic and Coordination Compounds, Theory and Applications in Inorganic Chemistry, John Wiley & Sons, 6(2008), p.109

15. **R. E. Smalley, L. Wharton, D. H. Levy,** Account of Chemical Research, 10(1977), p.139

16. **M. Dehghany, M. Afshari, J. Norooz Oliaee, N. Moazzen Ahmadi, A. R. W. McKellar,** Chemical Physics Letters, 473(2009), p.26

17. **J. Norooz Oliaee, M. Afshari, M. Dehghany, N. Moazzen Ahmadi, A .R .W . McKellar,** Chemical Physics Letters, 257(2009), p.133

18. **J. Norooz Oliaee, A. R. W. McKellar, N. Moazzen Ahmadi,** Chemical Physics Letters, 512(2011), p. 167

19. **D. G. Prichard, R. N. Nandi, J. S. Muenter, B. J. Howard,** The Journal of Chemical Physics, 89(1988), p.1245

20. **Z. S. Huang, R. E. Miller**, Chemical Physics, 132(1989), p.185

21. **J. S. Muenter,** The Journal of Chemical Physics, 90(1989), p.4048

22. **R. G. A. Bone, N. C. Handy,** Theoretica Chimica Acta, 78(1990), p.133

23. **J. S. Muenter,** The Journal of Chemical Physics, 94(1991), p.2781

24. **C. Lauzin, K. Didrich, J. Lievin, M. Herman, A. Perrin,** The Journal of Chemical Physics, 130(2009), p.204306

25. **C. Lauzin, J. Norooz Oliaee, M. Rezaei, N. Moazzen-Ahmadi,** Journal of Molecular Spectroscopy, 267(2011), p.19

26. **T. A. Hu, L. Sun, J. S. Muenter,** The Journal of Chemical Physics, 95(1991), p.1537

27. **A. D. Buckingham, P. W. Fowler,** Canadian Journal of Chemistry, 63(1985), p.2018

28. **A. J. Stone,** Chemical Physics Letters, 83(1981), p.233

29. **H. O. Leung,** Chemical Communications, (1996) , p.2525

30 **H. O. Leung,** The Journal of Chemical Physics, 107(1997), p.2232

31. **R. A. Peebles, S. A. Peebles, R. L. Kuczkowski and H. O. Leung,** The Journal of Chemical Physics, 103(1999), p.10813

32. **K. Didriche, C. Lauzin a, P. Mackoa, M. Hermana, W. J. Lafferty,** Chemical Physics Letters, 469(2009), p.36

33. **S. A. Peebles, R. L. Kuczkowski,** Journal of Physical Chemistry, 103(1999), p.3884

34. **S. A. Peebles, R. L. Kuczkowski,** Chemical Physics Letters, 312(1999), p.357

35. **S. A. Peebles, R. L. Kuczkowski,** Journal of Molecular Structure -THEOCHEM, 500(2000), p.391

36. **H. Valdés, J. A. Sordo,** Chemical Physics Letters, 387(2004), p.428

37. **P. R. Bunker, P. Jensen**, Molecular Symmetry and Spectroscopy, National Research Council of Canada, 2(2006)

38. **P. F. Bernath,** Spectra of Atoms and Molecules, Oxford University Press Inc, 2(2005)

39. **A. S. Kunju, G. Krishnan,** Group Theory and Its Application in Chemistry, PHI Learning Pvt. Ltd, (2010)

40. **L. D. Landau, E. M. Lifshitz,** Course of Thoeretical Physics, Pergamon Press Ltd., 3(2007)

41. **K. Sakai, A. Koide, T. Kihara,** Chemical Physics Letters, 47(1977), p.416

42.**R. D. Pendley, G. E. Ewing,** The Journal of Chemical Physics, 78(1983), p.3531

43. **R. E. Miller, P. F. Vohralik, R. O. Watts,** Journal of Chemical Physics, 80(1984), p.5453

44. **G. W. Bryant, D. F. Eggers, R. O. Watts,** Journal of the Chemical Society, 84(1988), p.1443.

45. **D. G. Prichard, R. N. Nandi, J. S. Muenter,** Journal of Chemical Physic , 89(1988), p.115

46. **T. Aoyama, O. Matsuoka, N. Nakagawa,** Chemical Physics Letters, 67(1979), p.508

47. **I. L. Alberts, T. W. Rowlands, N. C. Handy,** Journal of Chemical Physics, 88(1988), p.3811

48. **G.T. Fraser, R. D. Suenram, F. J. Lovas, A. S. Pine, J. T. Hougen, W. J. Lafferty, J. S. Muenter,** Journal of Chemical Physics, 89(1988), p.6028

49. **K. Didriche, C. Lauzin, T. Földes, D. Golebiowski, M. Herman,C. Leforestier,** Physical Chemistry Chemical Physics, 13(2010), p.14010

50. **J. Norooz Oliaee , N. Moazzen-Ahmadi, A. R. W. McKellar,** Jounrnal of Molecular Physics, 110(2012), p.2797

51. **W. Demtroder,** Laser Spectroscopy Basic Concepts and Instrumentation, Springer, 3(2003)

52. **A. R. Skinner, D. W. Chandler,** Amrican Journal of Physics, 48(1980), p.8

53. **Y. Bai, N. Bandyopadhyay, S. Tsao, S. Slivkin, M. Raseghi,** Applied Physics Letters, 98(2011), p.181102

54. **J. Faist, F. Cappasso, D. Sivco, C. Sirtori, A. Hutchinson, A. Cho,** Science, 264(1994), p.553

55. **Daylight Solutions,** http://www.daylightsolutions.com

56. **J. Faist,** Qunatum Cascade Lasers, Oxford University Press, 1(2013), p.107

57. **J. Devonson, O. Cathabard, A. N. Baranov,** Journal of Applied Physics, 91(2007), p.251102

58. **J. Devenson, R. Teissier, O. Cathabard, A. N. Baranov,** Applied Physical Letters, 90(2007), p.111118

59. **S. Kumar, B. S. Williams, Q. Hu, J. L. Reno,** Applied Physics Letters, 88(2006), p.121123

60. **M. Rochat, D. Hofstetter, M. Beck, J. Faist,** Applied Physics Letters, 75(2001), p.4271

61.**M. D. Brookes, C. Xia, J. Tang, J. A. Anstey, B. G. Fulsom, K. X. Au Yong ,J. M. King, A. R. W. McKellar,** Spectrochimica Acta. Part A, Molecular and biomolecular spectroscopy, 60(2004), p.3235

62. **J. B. McManus, P. L. Kebabian and M. S. Zahniser,** Applied Optics, 34(1995), p.3336

63. **C. M. Western,** Pgopher, a program for simulatin rotatipnal structure, University of Bristol, http://pgopher.ch.bris.ac.uk.

64. **Z. Kisiel**, http://www.ifpan.edu.pl/~kisiel/struct/struct.htm

65. **M. J. D. Powell,** The Computer Journal, 7(1964), p.155

66. **J. S. Muenter,** Final progress reports: Government Document, (2009)

67. **W. H. Press, B. P. Flannery, S. A. Teukolsky, W. T. Vetterling,** Numerical Recipes, 1989, p.297

68. **Z. Kisiel**, Journal of Molecluar Spectroscopy, 218(2003), p.58

69. **M. Dehghany, M. Afshari, N. Moazzen-Ahmadi, A. R. W. McKellar,** Physical Chemistry Chemical Physics, 10(2008), p.1658

Appendix 1

Calculated and observed transitions for a planar isomer of the N_2O – $(C_2H_2)_2$ trimer:

J''	**Ka''**	**K_c''**	**J'**	**K_a'**	**K_c'**	**Observed(cm^{-1})**	**Calculated(cm^{-1})**	**Obs.– Cal.**
0	0	0	1	0	1	2232.7470	2232.7472	-0.0001
1	1	0	2	1	1	2232.6714	2232.6708	0.0006
1	0	1	2	0	2	2232.6830	2232.6831	-0.0001
1	1	1	2	1	2	2232.6920	2232.6925	-0.0004
1	1	0	1	1	1	2232.8231	2232.8230	0.0001
1	0	1	0	0	0	2232.8774	2232.8776	-0.0002
2	1	1	3	1	2	2232.6007	2232.6008	-0.0001
2	2	1	3	2	2	2232.6161	2232.6158	0.0004
2	0	2	3	0	3	2232.6213	2232.6216	-0.0003
2	1	2	3	1	3	2232.6332	2232.6332	0.0000
2	1	2	2	1	1	2232.7801	2232.7795	0.0005
2	1	1	2	1	2	2232.8446	2232.8444	0.0002
2	1	2	1	1	1	2232.9316	2232.9317	-0.0001
2	0	2	1	0	1	2232.9414	2232.9413	0.0001
2	1	1	1	1	0	2232.9527	2232.9533	-0.0006
3	1	2	4	1	3	2232.5322	2232.5319	0.0003
3	2	1	4	2	2	2232.5385	2232.5385	0.0000
3	3	1	4	3	2	2232.5465	2232.5471	-0.0005
3	3	0	4	3	1	2232.5465	2232.5464	0.0001
3	2	2	4	2	3	2232.5504	2232.5512	-0.0008
3	0	3	4	0	4	2232.5634	2232.5632	0.0002
3	1	3	4	1	4	2232.5746	2232.5746	0.0000
3	2	1	3	2	2	2232.8176	2232.8180	-0.0004
3	1	3	2	1	2	2232.9903	2232.9905	-0.0002
3	0	3	2	0	2	2233.0024	2233.0022	0.0002
3	2	2	2	2	1	2233.0071	2233.0071	0.0000
3	2	1	2	2	0	2233.0130	2233.0125	0.0006
3	1	2	2	1	1	2233.0226	2233.0227	-0.0001
3	1	3	2	0	2	2233.0380	2233.0388	-0.0008
4	1	3	5	1	4	2232.4644	2232.4648	-0.0004
4	2	2	5	2	3	2232.4644	2232.4647	-0.0003
4	2	3	5	2	4	2232.4873	2232.4874	-0.0001
4	0	4	5	0	5	2232.5079	2232.5075	0.0004
4	2	3	4	2	2	2232.7920	2232.7914	0.0006
4	2	2	4	2	3	2232.8295	2232.8301	-0.0006

J''	Ka''	K_c''	J'	K_a'	K_c'	Observed(cm^{-1})	Calculated(cm^{-1})	Obs.– Cal.
4	1	4	3	1	3	2233.0483	2233.0483	0.0001
4	0	4	3	0	3	2233.0600	2233.0597	0.0002
4	2	3	3	2	2	2233.0712	2233.0708	0.0004
4	2	2	3	2	1	2233.0840	2233.0834	0.0006
4	1	3	3	1	2	2233.0909	2233.0907	0.0002
4	1	3	4	1	4	2232.9186	2232.9184	0.0002
4	1	4	4	1	3	2232.7036	2232.7038	-0.0003
4	2	3	5	2	4	2232.4874	2232.4874	0.0000
5	2	3	6	2	4	2232.3907	2232.3905	0.0001
5	2	4	6	2	5	2232.4245	2232.4246	-0.0001
5	0	5	6	0	6	2232.4535	2232.4532	0.0003
5	1	5	6	1	6	2232.4602	2232.4598	0.0004
5	2	3	5	2	4	2232.8524	2232.8521	0.0003
5	1	5	4	1	4	2233.1051	2233.1050	0.0000
5	0	5	4	0	4	2233.1144	2233.1144	0.0000
5	2	4	4	2	3	2233.1344	2233.1335	0.0009
5	1	4	4	1	3	2233.1564	2233.1566	-0.0002
5	2	3	4	2	2	2233.1564	2233.1561	0.0003
5	2	4	5	0	5	2233.1005	2233.1007	-0.0001
5	1	4	5	2	3	2232.6525	2232.6529	-0.0004
6	2	4	7	2	5	2232.3171	2232.3175	-0.0004
6	3	3	7	3	4	2232.3344	2232.3341	0.0003
6	1	5	7	1	6	2232.3392	2232.3392	-0.0001
6	2	5	7	2	6	2232.3631	2232.3629	0.0002
6	0	6	5	0	5	2233.1672	2233.1675	-0.0003
6	2	5	5	2	4	2233.1950	2233.1950	0.0000
6	3	3	5	3	2	2233.2113	2233.2111	0.0001
6	2	4	5	2	3	2233.2291	2233.2289	0.0002
6	1	6	5	1	5	2233.1609	2233.1609	0.0001
6	1	6	5	0	5	2233.1768	2233.1767	0.0000
6	3	4	5	3	3	2233.2047	2233.2054	-0.0007
6	2	4	6	1	5	2232.9764	2232.9764	0.0000
6	1	5	6	2	4	2232.6430	2232.6426	0.0004
6	1	6	6	2	5	2232.5006	2232.5007	-0.0001
7	2	6	8	2	7	2232.3021	2232.3024	-0.0003
7	2	6	6	2	5	2233.2551	2233.2551	0.0000
7	3	4	6	3	3	2233.2826	2233.2826	0.0000
7	2	5	6	2	4	2233.2999	2233.3002	-0.0003
7	0	7	6	0	6	2233.2198	2233.2201	-0.0003
8	1	7	9	1	8	2232.2264	2232.2266	-0.0002

J''	Ka''	K_c''	J'	K_a'	K_c'	Observed(cm^{-1})	Calculated(cm^{-1})	Obs.– Cal.
8	0	8	9	0	9	2232.2908	2232.2901	0.0007
8	1	8	9	1	9	2232.2908	2232.2914	-0.0006
8	2	7	7	2	6	2233.3138	2233.3139	-0.0001
8	2	6	8	1	7	2233.0299	2233.0305	-0.0007
8	1	7	7	1	6	2233.3349	2233.3349	0.0000
8	3	5	7	3	4	2233.3564	2233.3563	0.0001
8	5	4	9	4	5	2232.7584	2232.7583	0.0001
8	1	7	9	2	8	2232.1963	2232.1968	-0.0005
8	4	4	9	4	5	2232.2018	2232.2022	-0.0004
9	3	7	10	3	8	2232.1501	2232.1501	0.0000
9	1	8	10	1	9	2232.1739	2232.1730	0.0009
9	0	9	10	0	10	2232.2356	2232.2350	0.0006
9	1	9	10	1	10	2232.2356	2232.2357	-0.0001
9	0	9	8	0	8	2233.3252	2233.3257	-0.0005
9	1	9	8	1	8	2233.3252	2233.3243	0.0008
9	1	8	8	1	7	2233.3875	2233.3878	-0.0002
9	4	5	8	4	4	2233.4089	2233.4089	0.0000
9	4	6	8	4	5	2233.4042	2233.4037	0.0004
10	0	0	9	0	9	2233.3785	2233.3787	-0.0003
10	1	0	9	1	9	2233.3785	2233.3780	0.0004
10	1	9	9	1	8	2233.4388	2233.4391	-0.0004
10	1	9	9	1	8	2233.4386	2233.4391	-0.0005
10	2	8	9	2	7	2233.4976	2233.4969	0.0007
10	3	7	9	3	6	2233.5051	2233.5056	-0.0005
11	2	9	10	2	8	2233.5553	2233.5547	0.0006
11	3	8	11	3	9	2232.9806	2232.9806	0.0000

Appendix 2

Calculated and observed transitions for a planar isomer of the N_2O-$(C_2D_2)_2$ trimer:

J''	Ka''	K_c''	J'	K_a'	K_c'	Observed(cm^{-1})	Calculated(cm^{-1})	Obs.– Cal.
1	1	1	2	1	2	2232.8970	2232.8970	0.0000
1	0	1	2	0	2	2232.8884	2232.8882	0.0002
1	1	0	2	1	1	2232.8768	2232.8766	0.0002
1	1	0	1	1	1	2233.0196	2233.0197	-0.0001
2	1	2	1	1	1	2233.1223	2233.1220	0.0003
2	0	2	1	0	1	2233.1312	2233.1309	0.0003
2	1	1	1	1	0	2233.1423	2233.1423	0.0001
2	1	2	3	1	3	2232.8414	2232.8413	0.0002
2	0	2	3	0	3	2232.8303	2232.8304	-0.0001
2	2	1	3	2	2	2232.8250	2232.8248	0.0002
2	2	0	3	2	1	2232.8199	2232.8197	0.0002
2	1	1	3	1	2	2232.8108	2232.8108	0.0001
2	1	2	2	1	1	2232.9792	2232.9788	0.0004
2	0	2	2	1	1	2232.9343	2232.9337	0.0006
3	0	3	2	0	2	2233.1882	2233.1882	0.0000
3	2	2	2	2	1	2233.1928	2233.1928	0.0000
3	2	1	2	2	0	2233.1979	2233.1979	0.0000
3	1	2	2	1	1	2233.2078	2233.2075	0.0003
3	1	3	4	1	4	2232.7861	2232.7862	-0.0001
3	0	3	4	0	4	2232.7756	2232.7756	0.0000
3	2	2	4	2	3	2232.7640	2232.7641	-0.0001
3	2	1	4	2	2	2232.7520	2232.7521	-0.0001
3	1	2	4	1	3	2232.7459	2232.7460	-0.0002
3	1	3	2	1	2	2233.1772	2233.1772	0.0000
3	2	1	3	2	2	2233.0149	2233.0150	-0.0001
3	1	3	2	0	2	2233.2215	2233.2224	-0.0008
3	3	1	4	3	2	2232.7596	2232.7601	-0.0005
4	1	4	3	1	3	2233.2314	2233.2315	-0.0002
4	0	4	3	0	3	2233.2423	2233.2423	-0.0001
4	1	4	5	1	5	2232.7317	2232.7319	-0.0003
4	0	4	5	0	5	2232.7231	2232.7232	-0.0001
4	2	3	5	2	4	2232.7040	2232.7042	-0.0001
4	1	3	5	1	4	2232.6827	2232.6830	-0.0003
4	2	2	5	2	3	2232.6827	2232.6827	-0.0001
4	2	2	3	2	1	2233.2649	2233.2646	0.0002

J''	K_a''	K_c''	J'	K_a'	K_c'	Observed(cm^{-1})	Calculated(cm^{-1})	Obs.– Cal.
4	2	3	4	1	4	2233.2380	2233.2387	-0.0007
4	1	3	4	1	4	2233.1094	2233.1096	-0.0002
4	2	2	4	2	3	2233.0264	2233.0265	-0.0001
5	1	5	6	1	6	2232.6783	2232.6783	0.0000
5	0	5	6	0	6	2232.6723	2232.6722	0.0001
5	2	4	6	2	5	2232.6451	2232.6451	-0.0001
5	2	3	6	2	4	2232.6128	2232.6130	-0.0002
5	1	5	4	1	4	2233.2846	2233.2850	-0.0004
5	0	5	4	0	4	2233.2937	2233.2937	-0.0001
5	2	4	4	2	3	2233.3117	2233.3117	0.0000
5	2	4	5	2	3	2232.9679	2232.9679	0.0000
5	3	2	6	3	3	2232.6285	2232.6286	-0.0001
5	1	5	4	0	4	2233.3081	2233.3085	-0.0004
5	1	4	5	0	5	2233.1728	2233.1725	0.0002
5	1	4	5	2	3	2232.8611	2232.8603	0.0008
5	1	5	6	0	6	2232.6872	2232.6870	0.0002
5	0	5	6	1	6	2232.6630	2232.6636	-0.0006
6	2	5	7	2	6	2232.5872	2232.5872	0.0000
6	1	5	7	1	6	2232.5650	2232.5650	-0.0001
6	3	3	7	3	4	2232.5596	2232.5598	-0.0002
6	1	6	5	1	5	2233.3373	2233.3375	-0.0001
6	0	6	5	0	5	2233.3434	2233.3436	-0.0002
6	2	5	5	2	4	2233.3694	2233.3695	-0.0001
6	3	3	5	3	2	2233.3847	2233.3847	-0.0001
6	2	4	5	2	3	2233.4016	2233.4015	0.0001
6	1	6	7	1	7	2232.6252	2232.6253	-0.0001
6	2	4	7	2	5	2232.5443	2232.5444	0.0000
6	2	5	6	1	6	2233.2976	2233.2974	0.0002
6	3	3	6	2	4	2233.2595	2233.2596	-0.0001
6	3	4	5	3	3	2233.3787	2233.3793	-0.0006
7	1	7	6	1	6	2233.3892	2233.3893	-0.0001
7	2	6	6	2	5	2233.4261	2233.4261	0.0000
7	3	4	6	3	3	2233.4518	2233.4521	-0.0002
7	1	6	6	1	5	2233.4487	2233.4486	0.0001
7	2	5	6	2	4	2233.4687	2233.4686	0.0000
7	3	5	7	3	4	2232.9861	2232.9858	0.0003
7	2	6	8	2	7	2232.5302	2232.5303	-0.0001
7	2	5	8	2	6	2232.4777	2232.4778	-0.0001
7	3	4	8	3	5	2232.4888	2232.4887	0.0000

J''	K_a''	K_c''	J'	K_a'	K_c'	Observed(cm^{-1})	Calculated(cm^{-1})	Obs.– Cal.
7	1	6	6	2	5	2233.3640	2233.3637	0.0003
7	0	7	6	0	6	2233.3928	2233.3931	-0.0003
7	1	7	6	0	6	2233.3982	2233.3979	0.0003
8	2	7	7	2	6	2233.4811	2233.4814	-0.0002
8	3	5	7	3	4	2233.5214	2233.5215	-0.0001
8	2	7	9	2	8	2232.4747	2232.4746	0.0001
8	1	7	9	1	8	2232.4594	2232.4593	0.0000
8	4	4	9	4	5	2232.4358	2232.4358	0.0001
8	3	6	9	3	7	2232.4475	2232.4475	0.0000
9	0	9	8	0	8	2233.4920	2233.4925	-0.0005
9	1	9	8	1	8	2233.4920	2233.4913	0.0007
9	1	8	8	1	7	2233.5507	2233.5508	-0.0001
9	0	9	10	0	10	2232.4677	2232.4673	0.0004
9	1	9	10	1	10	2232.4677	2232.4679	-0.0002
9	3	7	10	3	8	2232.3872	2232.3871	0.0001
9	2	7	10	2	8	2232.3537	2232.3535	0.0002
9	3	6	10	3	7	2232.3442	2232.3441	0.0001
9	2	8	10	2	9	2232.4197	2232.4197	0.0000
10	0	10	9	0	9	2233.5421	2233.5425	-0.0003
10	1	10	9	1	9	2233.5421	2233.5418	0.0003
10	1	9	11	1	10	2232.3586	2232.3587	-0.0001
10	2	9	9	2	8	2233.5885	2233.5882	0.0003
10	1	9	9	1	8	2233.5990	2233.5991	-0.0001
10	4	7	10	3	8	2233.4312	2233.4322	-0.0010
10	2	9	10	1	10	2233.4646	2233.4651	-0.0005
10	3	7	9	3	6	2233.6621	2233.6619	0.0001
10	2	8	9	2	7	2233.6525	2233.6535	-0.0010
11	1	10	10	1	9	2233.6471	2233.6471	0.0000

Appendix 3

Calculated and observed transitions for a planar isomer of the $^{15}N_2O$-$(C_2H_2)_2$ trimer:

J''	K_a''	K_c''	J'	K_a'	K_c'	Observed(cm^{-1})	Calculated(cm^{-1})	Obs.– Cal.
0	0	0	1	0	1	2163.3449	2163.3445	0.0004
1	1	0	2	1	1	2163.2699	2163.2699	-0.0001
1	0	1	2	0	2	2163.2817	2163.2817	-0.0001
1	1	1	2	1	2	2163.2905	2163.2908	-0.0003
1	0	1	0	0	0	2163.4722	2163.4722	0.0000
2	2	0	3	2	1	2163.2107	2163.2110	-0.0003
2	2	1	3	2	2	2163.2165	2163.2160	0.0005
2	0	2	3	0	3	2163.2217	2163.2213	0.0004
2	1	2	3	1	3	2163.2324	2163.2327	-0.0003
2	1	1	2	1	2	2163.4392	2163.4393	-0.0001
2	1	2	1	1	1	2163.5253	2163.5255	-0.0002
2	1	1	1	1	0	2163.5463	2163.5463	0.0000
3	1	2	4	1	3	2163.1340	2163.1339	0.0001
3	0	3	4	0	4	2163.1639	2163.1639	-0.0001
3	1	3	4	1	4	2163.1752	2163.1752	0.0000
3	1	3	2	1	2	2163.5831	2163.5832	-0.0001
3	0	3	2	0	2	2163.5945	2163.5945	0.0000
4	1	3	5	1	4	2163.0683	2163.0681	0.0002
4	2	3	5	2	4	2163.0899	2163.0903	-0.0004
4	0	4	5	0	5	2163.1090	2163.1092	-0.0002
4	1	4	5	1	5	2163.1186	2163.1185	0.0001
4	1	3	4	1	4	2163.5111	2163.5108	0.0003
4	1	4	3	1	3	2163.6399	2163.6399	0.0000
4	0	4	3	0	3	2163.6516	2163.6512	0.0004
5	2	3	6	2	4	2162.9964	2162.9962	0.0002
5	3	2	6	3	3	2163.0128	2163.0127	0.0001
5	2	4	6	2	5	2163.0287	2163.0287	0.0000
5	0	5	6	0	6	2163.0564	2163.0558	0.0005
5	1	5	6	1	6	2163.0630	2163.0625	0.0004
5	1	5	4	1	4	2163.6959	2163.6958	0.0001
5	0	5	4	0	4	2163.7050	2163.7051	-0.0001
5	2	4	4	2	3	2163.7228	2163.7233	-0.0006
5	1	4	4	1	3	2163.7451	2163.7455	-0.0004
6	2	4	7	2	5	2162.9248	2162.9246	0.0002
6	1	5	7	1	6	2162.9451	2162.9446	0.0005

J''	K_a''	K_c''	J'	K_a'	K_c'	Observed(cm^{-1})	Calculated(cm^{-1})	Obs.– Cal.
6	2	5	7	2	6	2162.9684	2162.9681	0.0002
6	1	6	5	1	5	2163.7502	2163.7508	-0.0005
6	0	6	5	0	5	2163.7571	2163.7574	-0.0003
6	2	5	5	2	4	2163.7837	2163.7837	-0.0001
6	3	3	5	3	2	2163.7991	2163.7990	0.0001
6	2	4	5	2	3	2163.8157	2163.8158	-0.0001
7	2	6	8	2	7	2162.9087	2162.9087	0.0000
7	2	5	7	2	6	2163.5194	2163.5200	-0.0006
7	2	6	6	2	5	2163.8427	2163.8429	-0.0001
8	2	7	9	2	8	2162.8500	2162.8504	-0.0005
8	2	7	7	2	6	2163.9005	2163.9007	-0.0002
9	3	6	10	3	7	2162.7172	2162.7173	0.0000
9	3	7	10	3	8	2162.7597	2162.7603	-0.0006
9	1	8	10	1	9	2162.7810	2162.7809	0.0001
9	0	9	10	0	10	2162.8420	2162.8420	0.0000
9	2	7	9	2	8	2163.6335	2163.6330	0.0004
9	1	9	8	1	8	2163.9123	2163.9118	0.0005
9	1	8	8	1	7	2163.9740	2163.9739	0.0001
9	4	5	8	4	4	2163.9935	2163.9929	0.0006
10	2	8	11	2	9	2162.6648	2162.6647	0.0002
10	2	9	9	2	8	2164.0129	2164.0127	0.0002
10	2	8	9	2	7	2164.0795	2164.0797	-0.0002
11	2	9	12	2	10	2162.6083	2162.6085	-0.0002
11	1	10	10	1	9	2164.0755	2164.0750	0.0005
11	3	9	10	3	8	2164.1035	2164.1038	-0.0003
13	1	13	14	1	14	2162.6242	2162.6244	-0.0002